12

Mathematical Modeling of Multi-Element Infrared Focal Plane Arrays Based on the System 'Photodiode – Direct-Injection Readout Circuit'

I.I. Lee and V.G. Polovinkin
A.V. Rzhanov Institute of Semiconductor Physics Siberian Branch of Russian Academy of Sciences
Russia

1. Introduction

The direct-injection readout circuit was proposed in 1973 by A. Steckl and T. Koehler (Steckl & Koehler, 1973). With such readout circuits, first hybrid multi-element InfraRed Focal Plane Arrays (IR FPAs) were implemented (Steckl, 1976; Iwasa, 1977). The direct-injection readout circuits are being used in the majority of hybrid multi-element Long-Wave InfraRed (LWIR) FPAs, which hold more-than-70% a share in the world market of thermography systems (Rogalski, 2000).

A diagram of FET-based readout circuit is shown in Fig.1a, the most popular design involving a charge-coupled device, Fig.1b (Longo, 1978; Felix,1980; Takigawa, 1980; Rogalski, 2000). On application of a dc voltage U_G to the input gate, a certain voltage, defined by the surface potential under the input gate of the photodetector channel, sets across the photodiode, and the current generated in the IR detector is integrated at the storage capacitor C_{int}. On applying of a transfer pulse Ft (Fig.1a), the charge accumulated in the storage capacitor transfer to the column read bus.

The equivalent circuit of the direct injection readout circuit is shown in Fig. 2.

Normally, the current through the photodiode is in the range of $10^{-7}\div10^{-10}$A, the input FET being therefore operated in subthreshold mode. The transconductance of the input FET channel is:

$$g_{in} = \frac{\partial I_{in}}{\partial V_G} = \frac{qI_{in}}{N^* kT} \tag{1}$$

Here, q is the electron charge, k is the Boltzmann constant, $N^* = (C_{OX}+C_D^*+C_{SS}^*)/C_{OX}$ (C_{OX} is the specific capacitance of gate dielectric, $C_{SS}^*=qN_{ss}^*$ is the specific capacitance of fast surface states, C_D^* is the specific capacitance of the depletion region, T is temperature, and the asterisk * indicates that the parameter value is taken for the conditions with surface Fermi level equal to $3/2\ \varphi_{FB}$.

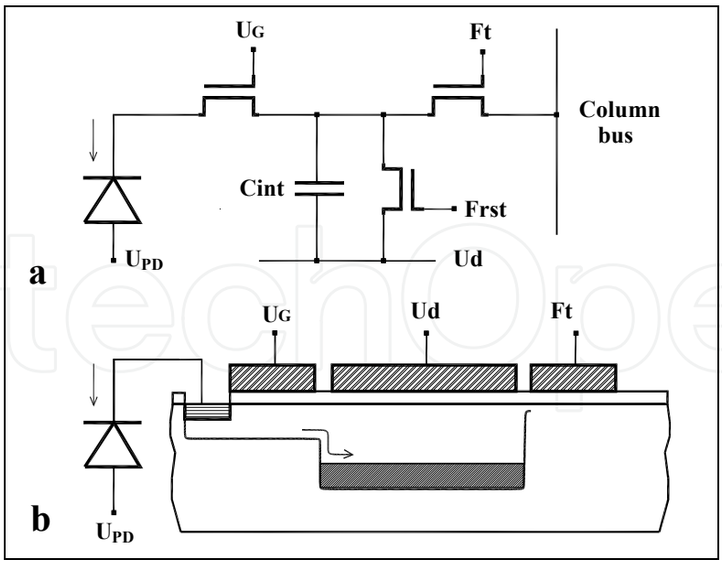

Fig. 1. Readout circuit with charge direct injection.

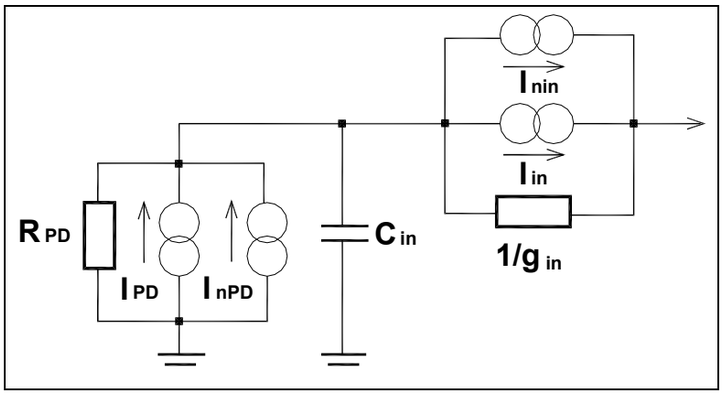

Fig. 2. The equivalent circuit of the photodetector channel of a hybrid IR FPA based on the system 'photodiode – direct-injection readout circuits'. Here, I_{PD} is the current that flows through the photodiode, I_{nPD} is the noise current that flows through the photodiode, R_{PD} is the dynamic resistance of the photodiode, I_{in} is the current integrated under the storage gate of the readout circuit, I_{nin} is the noise current integrated under the storage gate, and C_{in} is the capacitance of the input direct injection.

From the equivalent circuit, all basic relations for the readout circuit of interest can be inferred. In particular, for injection efficiency η_I we obtain (Longo, 1978; Felix,1980):

$$\eta_I = \frac{g_{in}}{g_{PD}+g_{in}+j\omega C_{in}} \tag{2}$$

where $g_{PD}=1/R_{PD}$, R_{PD} is the dynamic resistance of the photodiode.

Analysis of transfer characteristics of the system 'photodiode – direct-injection readout circuit' has revealed several drawbacks inherent to such readout circuits (Longo, 1978; Felix,1980; Takigawa, 1980; Rogalski, 2000):

- an IR FPA responsivity value comparable with that of IR photodiodes operated in photovoltaic regime can be reached only on the condition that the injection efficiency approaches unity. This requirement entails rigid requirements on the dynamic resistance of photodiodes, these requirements often being hard to meet, especially in LWIR FPAs;
- since the bias voltage across the photodiode is defined by the surface potential of the input-gate modulated channel, for multi-element IR FPAs the variations of transfer characteristics (fixed-pattern noise) and the excess noise level proved to be largely defined by the spread of input-FET threshold voltages ΔV_{th} (Longo, 1978; Gopal, 1996).

Several circuit designs were proposed to eliminate the above drawbacks. For instance, R. Bluzer and R. Stehlik (Bluzer & Stehlik,1978) proposed to use, with the aim of reducing the input impedance of readouts, the so-called buffered direct injection, implemented through introduction of an inverting amplifier in between the input direct injection and input FET gate.

J. Longo *et al.* (Longo, 1978) proposed a design of direct injection readout circuit capable of diminishing the spread of photodiode bias voltages to the typical difference of threshold voltages of two closely spaced FETs. Nonetheless, being capable of improving certain characteristics of direct injection readouts, the additional components (the amplifier normally involves 4 to 6 FETs) take off a substantial fraction of surface area from the photodetector cell, doing simultaneously the direct injection readout circuits out of their main advantageous features, low energy consumption and a large storage capacity, high in comparison with readout circuits of other types.

The advances in silicon technology and in the technology of IR photodiodes based on narrow bandgap semiconductors have allowed a substantial increase of photodiode dynamic resistance and a reduced variation of photodiode bias voltages across FPA from the values ~ 20-50 mV, typical of the technology level of the 1970s, to ~ 1-10 mV. For this reason, as a rule, the simplest design of direct injection readout circuit shown in Fig.1 is mainly used.

An analysis of the system 'photodiode – direct injection readout circuit' given in (Steckl & Koehler 1973; Steckl, 1976; Iwasa, 1977; Rogalski, 2000; Longo, 1978; Felix,1980; Takigawa, 1980; Gopal, 1996) was carried out versus photodiode biasing, although the bias voltage across the photodiode is defined by the surface potential in the input-FET channel and can be adjusted through the proper choice of the potential U_G applied to the input-FET gate. That is why such estimates do not allow the prediction of responsitivity of multi-element IR FPAs and evaluation of fixed-pattern noise level and Noise-Equivalent Temperature Difference (NETD) figures of thermography systems based on such IR FPAs. In other words, such estimates do not permit numerical modeling of multi-element IR FPAs.

In the present article, we propose a mathematical model of the system 'photodiode – direct injection readout circuit', a computer program, and an analysis procedure for thermography systems based on multi-element IR FPAs; these model and analysis procedure were developed to solve the above-indicated problems. We describe a procedure for revealing the effects due to the spread of electrophysical parameters of photodiodes and Si readouts based on plotting calculated fixed-pattern noise, detectivity, and NETD histograms of thermography systems based on multi-element IR FPAs. It is significant that all

dependences were obtained as dependent on the input-gate voltage of readouts; this enables a comparison with the experiment and formulation of requirements to electrophysical and design parameters of photodiodes and Si readouts necessary for implementation of design characteristics.

2. A mathematical model for the system 'IR photodiode - direct-injection readout circuit'

Basic assumptions adopted in the proposed mathematical model of the system 'IR photodiode – direct injection readout circuit' were first formulated in (Kunakbaeva, Lee & Cherepov, 1993) and further developed in (Kunakbaeva & Lee, 1996; Karnaushenko; Lee et al., 2010; Gumenjuk-Sichevska, Karnaushenko, Lee & Polovinkin, 2011). In calculating the transfer characteristics of the system, for the input FET we employ the model of long-channel transistor in weak inversion (Overstraeten, 1975). The noise charge Q(t) integrated under the storage gate of the direct injection readout circuit is calculated as a McDonalds function expressed in terms of spectral current density $S_i(\omega)$ (Buckingham, 1983):

$$\overline{Q^2}(t) = \frac{1}{\pi}\int_0^{\infty} \frac{S_i(\omega)}{\omega^2}(1-\cos\omega t)d\omega \tag{3}$$

The spectral density of the noise current in the input-gate modulated channel is given by

$$S_i(\omega) = 4kTg_{in}\alpha_1\left|1-\eta_I\right|^2 + \frac{2\pi B_{in}I^2{}_{in}}{\omega}\left|1-\eta_I\right|^2 + \left(2qI_{PD} + \frac{4kT\alpha_2}{R_{PD}}\right)\left|\eta_I\right|^2 + \frac{2\pi B_{PD}}{\omega}\left|\eta_I\right|^2 \tag{4}$$

The first and second terms in (4) stand for the thermal noise of the input FET and for the 1/f noise induced by this FET (here, α_1 and α_2 are coefficients) and the third and forth terms stand for the thermal noise and 1/f noise of the photodiode, here, $B_{in}= 2\pi KI_{in}^2/WL(C_{OX}+C_D^*)^2$, K is a coefficient (D'Souza, 2002), and $B_{PD} = \alpha_3\left(I_{PD} - \eta_K I_P\right)^2$, α_3 is a coefficient (Tobin, 1980). Substituting the first term of (4) into (3), after integration we obtain the following analytical expression for Q_1 - the thermal noise of the gate-modulated channel expressed as the amount of noise electrons:

$$\begin{aligned} Q_1^2 = {} & \frac{2kTC_{in}g_{in}R_{PD}\alpha_1}{q^2(1+g_{in}R_{PD})}\left[1-\exp\left(-T_{in}\frac{1+g_{in}R_{PD}}{R_{PD}C_{in}}\right)\right] + \\ & + \frac{2kTg_{in}\alpha_1}{q^2(1+g_{in}R_{PD})^2}\left[T_{in} - \frac{R_{PD}C_{in}}{1+g_{in}R_{PD}}\left(1-\exp\left(-T_{in}\frac{1+g_{in}R_{PD}}{R_{PD}C_{in}}\right)\right)\right] \end{aligned} \tag{5}$$

where T_{in} is the integration time.

In estimating the 1/f noise of the input FET Q_2, also expressed as the amount of noise electrons, while performing integration, we have to take the fact into account that the readout regime involves a high-pass filter with transfer characteristic $\omega^2/(\omega_0^2 + \omega^2)$, where $\omega_0 = \pi/T_{in}$.

$$Q_2^2 = \frac{2KI_{in}^2}{qWL(C_{OX}+C_D)^2}\int_0^\infty \frac{1+(C_{in}R_{PD}\omega)^2}{(1+g_{in}R_{PD})^2+(C_{in}R_{PD}\omega)^2}\frac{1}{\omega(\omega_0^2+\omega^2)}\sin^2\frac{\omega T_{in}}{2}d\omega \quad (6)$$

We substitute the third term of (4) into (3) and obtain, after integration, the following analytical expression for Q_3 - the noise component due to photodiode current noise expressed as the amount of noise electrons:

$$Q_3^2 = \frac{(g_{in}R_{PD})^2}{q^2(1+g_{in}R_{PD})^2}\left(qI_{PD}+\frac{2kT\alpha_2}{R_{PD}}\right)\left(T_{in}-\frac{R_{PD}C_{in}}{1+g_{in}R_{PD}}\left(1-\exp\left(-T_{in}\frac{1+g_{in}R_{PD}}{R_{PD}C_{in}}\right)\right)\right) \quad (7)$$

The forth term in (4) stands to allow for the 1/f noise of the photodiode:

$$Q_4^2 = 2\alpha_3^2(I_{PD}-\eta_K I_P)^2\frac{(g_{in}R_{PD})^2}{q^2}\cdot \cdot\int_0^\infty \frac{1}{\left(1+g_{in}R_{PD}\right)^2+\left(C_{in}R_{PD}\omega\right)^2}\frac{1}{\omega\left(\omega_0^2+\omega^2\right)}\sin^2\frac{\omega T_{in}}{2}d\omega \quad (8)$$

The detectivity D* of the photodetector channel in which photosignals from the IR photodiode are read into the direct injection input is given by (Rogalski, 2000):

$$D^* = \frac{\lambda}{\hbar c}\frac{(A_{PD}T_{in}/2)^{1/2}\eta_I\eta_K}{\left(Q_1^2+Q_2^2+Q_3^2+Q_4^2+Q_{other}^2\right)^{1/2}} \quad (9)$$

where A_{PD} is the photodiode area and Q_{other} stands for all other noise components such as, for instance, the measuring channel induced noise.

3. Examples of model calculations

3.1 Modeling procedure for multi-element IR FPAs with direct injection readout circuits

The modeling procedure for the system 'IR photodiode – direct injection readout circuits' can be described using the simple IR photodiode model:

$$I_{PD} = \eta_K I_P + I_0\left[1-\exp(-\beta V_{PD})\right]+\frac{V_{PD}}{R_S} \quad (10)$$

Here, η_κ is photodiode quantum efficiency, I_0 is the photodiode saturation current, R_S is the photodiode shunt resistance, and I_P is the current induced by background radiation.

The calculation starts with specifying the values of electrophysical and design parameters of readout circuits, photoelectrical parameters of photodiodes, and operating conditions of IR FPA, which all are listed in Table. 1.

At a given input gate voltage V_G, the voltage across the photodiode can be determined from the condition $I_{in} = I_{PD}$. We identify the points of intersection of the current-voltage

characteristic of the photodiode and the transfer characteristics of the input FET to determine the photodiode bias voltage.

Designation	Parameter	Numerical value
μ	Mobility of minorities in the inversion channel of FET	500 $cm^2 V^{-1} \cdot c^{-1}$
N_D	Donor concentration in the substrate	$7 \cdot 10^{14}$ cm^{-3}
C_{OX}	Specific capacitance of gate dielectric	$1.24 \cdot 10^{-7}$ $F \cdot cm^{-2}$
V_{FB}	Flat-band voltage	0 V
N_{ss}^{*}-	Surface-state density	$1 \cdot 10^{9}$ $cm^{-2} \cdot eV^{-1}$
W, L	Length and width of input-gate modulated channel	30 μm, 3 μm
C_{in}	Input capacitance of FPA cell	0.5 pF
α_1	Numerical coefficients	2
α_2	Numerical coefficients	2
α_3	Numerical coefficients	10^{-3}
K	Numerical coefficients	$1.5 \cdot 10^{-24}$ $F^2 \cdot cm^{-2}$
A_{PD}	Photodiode area	$9 \cdot 10^{-5}$ cm^2
η_K	Photodiode quantum efficiency	0.8

Table 1. Design and electrophysical parameters of readout circuits

Figure 3 shows the curves of currents I_{in} and I_{PD} for the photodiode model (10). With the parameters of photodiode, input FET, and radiation environment adopted in Fig. 3, the voltage drop across the photodiode is zero at V_{G0} = 1.198 V. Given the voltage V_G, the quantities η_I, I_{in}, and D^* can be calculated. In the next cycle, a new value is assigned to V_G, and all the characteristics are to be recalculated. In this way, we obtain the main performance characteristics of the system 'photodiode-direct injection readout' as a function of the gate voltage at the input gate. The dependences in Fig. 3 can be used in a joint analysis of the effect due to noise characteristics of photodiodes, measured versus photodiode bias voltage, and the responsivity of photodetector channels based on the system 'photodiode – direct injection readout circuits'.

Figures 4a, b, c, and d shows the calculated curves of photodiode bias voltage $V_{PD}(V_G)$, injection efficiency $\eta_I(V_G)$, input current $I_{in}(V_G)$, and detectivity $D^*(V_G)$, respectively.

At V_{PD} = 0 V, the product $g_{in}R_{PD}$ for curves 1-5 in Fig. 4 equals respectively 794, 11.1, 11.1, 3.4, and 1.4. As it is seen from Figs. 4a and 4b, the dependences $V_{PD}(V_G)$ and $\eta_I(V_G)$ small informative in evaluating the uniformity level of transfer characteristics and responsivities of photodetector channels, more helpful here being the dependences $I_{in}(V_G)$ and $D^*(V_G)$ (see Figs 4c and 4d). As it is seen from Fig. 4, curves 1, at $g_{in}R_{PD}$ >100 the photodiode-direct injection readout system can be considered "ideal". With increasing the gate voltage V_G, as the photodiode bias voltage approaches zero, the injection efficiency η_I tends to unity, the current integrated in the readout circuit becomes roughly equal to I_{PD}, $I_{in} \approx I_{PD}$, and the detectivity reaches $D^* \approx 2.87 \cdot 10^{11}$ $cm \cdot Hz^{1/2} \cdot Wt^{-1}$, this value being comparable with the theoretical limit of D^* for a photodiode with η_K=0.8 operating in photovoltaic regime in BLIP mode. With further increase of V_G, for the "ideal" system the performance characteristics of the photodetector channel based on the system 'photodiode – direct injection readout circuit' (namely, η_I, I_{in}, and D^*) become almost independent of both V_G and electrophysical and design parameters of readout circuits. In the latter case, performance

characteristics of IR FPAs based on direct injection readout circuits can be evaluated using standard simplifications (Longo, 1978; Felix,1980). In "non-ideal" systems, in which the relation $g_{in}R_{PD}$ >>1 is fulfilled not too strict (see curves 2-5 in Figs. 4c and 4d), curves I_{in} (V_G) and D*(V_G) show a different behavior. The current I_{in} integrated in the readout circuit increases with increasing V_G. The dependences D*(V_G) exhibit a pronounced maximum. Being considered as a function of photodiode electrophysical parameters and background illumination current, the maximum detectivity is attained at a voltage V_G at which the photodiode gets driven by 5-30 mV in reverse direction (curve 4 in Fig. 4); this detectivity rather weakly depends on the value of $g_{in}R_{PD}$. For instance, as the value of $g_{in}R_{PD}$ decreases from 794 to 3.4 (curves 1 and 4 in Fig. 4) the detectivity D* falls in value from $2.87 \cdot 10^{11}$ cm $\cdot Hz^{1/2} \cdot Wt^{-1}$ to $1.96 \cdot 10^{11}$ cm $\cdot$ $Hz^{1/2} \cdot Wt^{-1}$, i.e. within a factor of 1.5. Note that the values of $g_{in}R_{PD}$ for curves 2 and 3 are identical; nonetheless, the dependences I_{in} (V_G) (Fig. 4c) and D* (V_G) (Fig.4d) for those cases differ substantially.

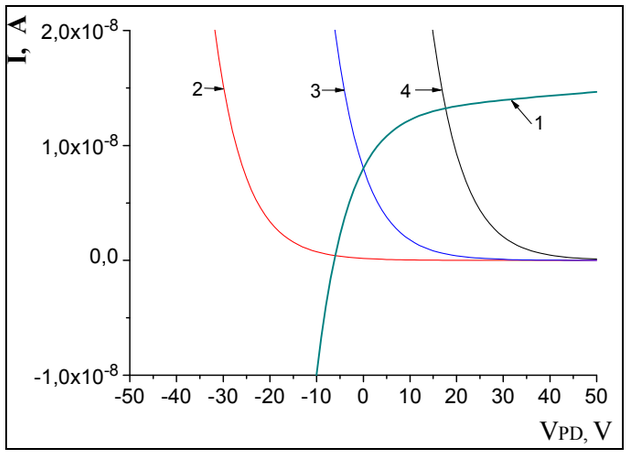

Fig. 3. Current-voltage characteristics of photodiode (curve 1) and input FET in weak inversion (curves 2-4) for three values of V_G, 1.17, 1.198, and 1.22 V. $I_0=5 \cdot 10^{-9}$ A, $R_S=3 \cdot 10^7$ Ohm, $I_P = 1 \cdot 10^{-8}$ A, and η_K =0.8.

The factors causing these differences can be clarified if one considers the calculated dependences of Fig. 5; in this figure, in addition to curves D* (V_G), also dependences $Q_1(V_G)$, $Q_2(V_G)$, $Q_3(V_G)$, and $Q_4(V_G)$ are shown. In the "ideal" system (see Fig.5 a), with increasing the voltage V_G, when the injection efficiency approaches unity, the total noise charge Q_5 becomes defined just by the photodiode noise current Q_3, having almost the same magnitude as the noise induced by background radiation fluctuations (9) since $I_{in} \approx I_P$ and $\eta_I \approx 1$. In "non-ideal" systems (see calculated dependences in Fig. 5 b-e), the charge Q_5 grows in value with increasing V_G. The increase of the noise and the related reduction of D* is primarily defined by the growth of Q_3 and Q_4. For the dependences shown in Fig. 5 b-e the difference between the curves D*(V_G) is primarily defined by the growth of the 1/f noise of photodiode (component Q_4). The difference of the dependences $Q_4(V_G)$ is due to the higher current I_{in} and a lower value of η_I for curves 4. With identical values of $g_{in}R_{PD}$ at zero voltage drop across the photodiode (compare Fig. 5b and Fig. 5c), a better IR FPA responsivity can be reached with diodes exhibiting a larger dynamic resistance on their biasing in reverse direction by 10-30 mV. For state-of-the-art level of silicon technology (C_{ox} ~ $(0.5\text{-}1.2) \cdot 10^{-7}$ F $\cdot cm^{-2}$, N*≈ 1), the noise induced by the input FET (cp. curves 1 and 2) is only substantial at

voltages $V_G < V_{G0}$ even if the product $g_{in}R_{PD}$ has a value close to unity, and this noise does not limit the IR FPA detectivity. Knowing of the values of individual noise components enables goal-directed optimization of electrophysical and design parameters of photodiodes and readout circuits.

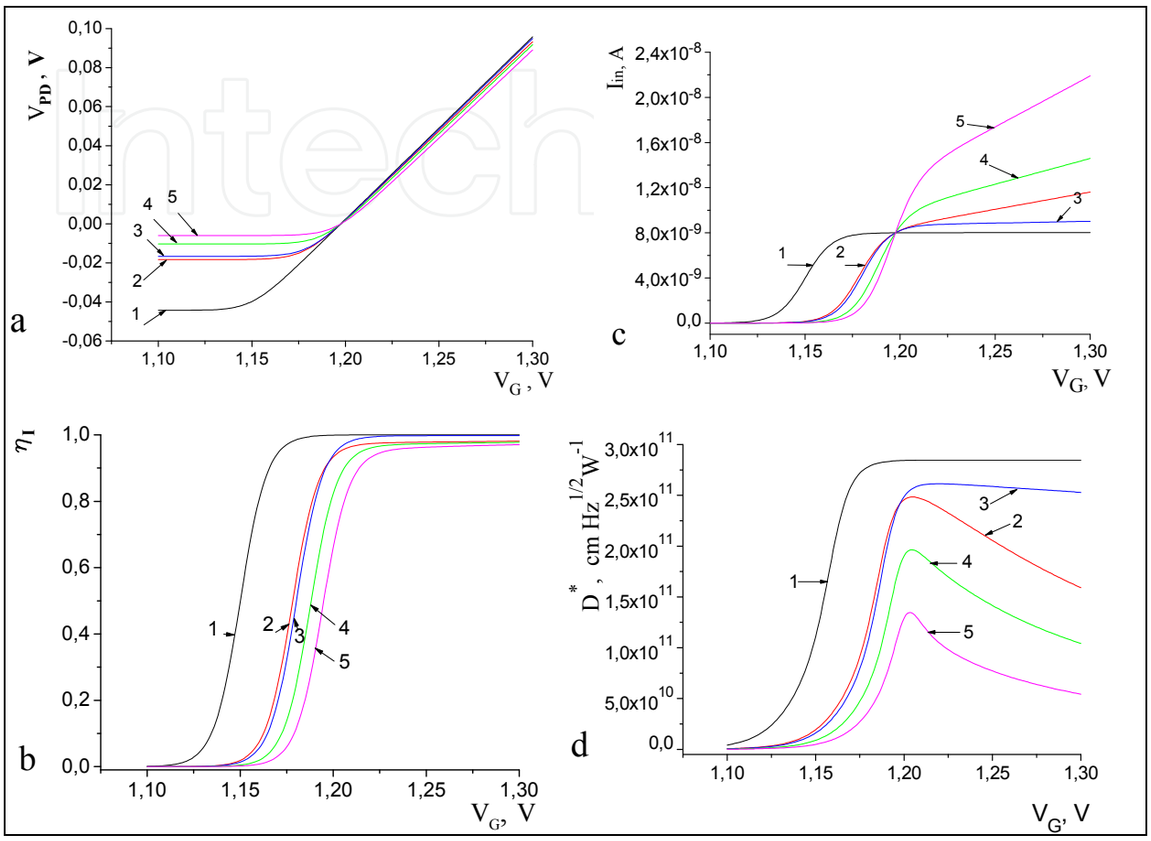

Fig. 4. Calculated dependences of performance characteristics of a photodiode-direct injection system on input-gate voltage. a – photodiode bias voltage, b – injection efficiency η_I, c – current I_{in} integrated in the readout circuit, d - detectivity D*. Integration time T_{in} =5 ·10^{-4} s, I_P =1 ·10^{-8} A, η_K =0.8, for curve 1 - I_0 =1 ·10^{-11} A, R_P=1 ·10^{11} Ohm; for curve 2 - I_0 =5 ·10^{-10} A, R_P =3 ·10^7 Ohm; for curve 3 - I_0 =7 ·10^{-10} A, R_P =3 ·10^8 Ohm; for curve 4 - I_0 = 2 ·10^{-9} A, R_P = 2 ·10^7 Ohm; for curve 5 - I_0 = 5 ·10^{-9} A, R_P =1 ·10^7 Ohm.

Important figures of merit of multi-element IR FPAs are the fixed-pattern noise and the responsivity uniformity of photodetector channels. The spread of photoelectric parameters is defined by the variation of electrophysical parameters of readouts and by the variation of photoelectrical parameters of photodiodes. For direct injection readouts operated in weak inversion regime, the main effect is due to input-FET threshold variations rather than due to non-uniformity of geometric dimensions of input-FET gates.

Histograms of photodiode bias voltages and injection efficiencies calculated with allowance for FET threshold variations are shown in Fig. 6. In performing the calculations, it was assumed that the spread of threshold voltages obeys a normal distribution law, and a total of 1000 realizations were considered. As it is seen from Fig. 6, the spread of FET threshold voltages leads to a spread of photodiode bias voltages (Fig. 6 a), and also to a spread of

injection efficiencies η_I and, as a consequence, to variation of transfer characteristics of the 'photodiode-direct injection readout' system.

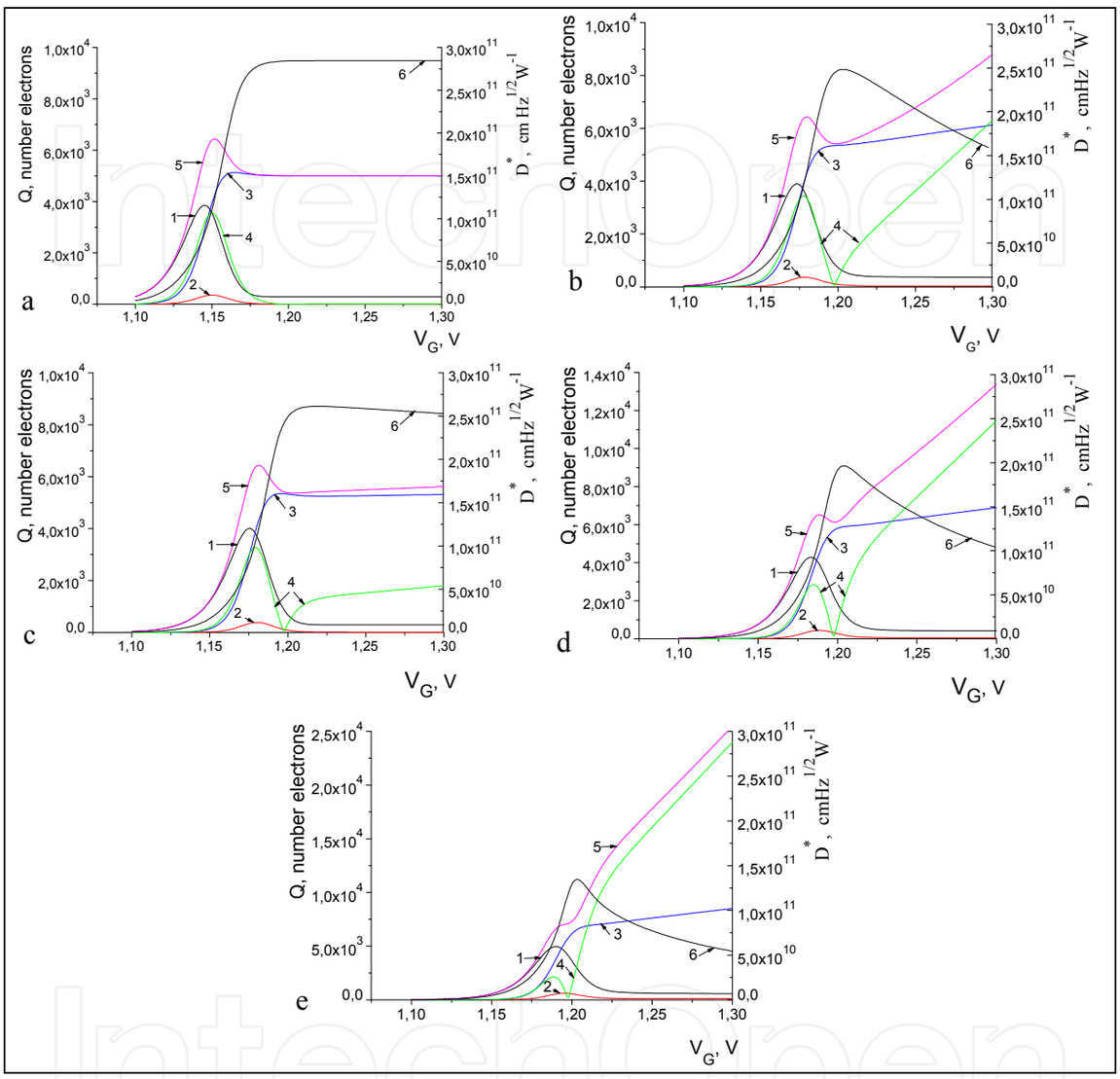

Fig. 5. Calculated dependences of $D^*(V_G)$ (curve 6, right axis) and $Q_1(V_G)$, $Q_2(V_G)$, $Q_3(V_G)$, $Q_4(V_G)$, and $Q_5(V_G)$ (curves 1-5, left axis). $Q_5=(Q_1^2+Q_2^2+Q_3^2+Q_4^2)^{1/2}$. The values of photodiode electrophysical parameters adopted in the calculations are the same as in Fig. 4 for curves 1-5, respectively.

Figure 7 shows the calculated curve $I_{in}(V_G)$ that illustrate the influence of the dispersion of threshold voltages with $\sigma(V_{th})$ = 10 mV on the characteristics of a multi-element IR FPA (the values of photoelectrical parameters for IR photodiodes are the same as those adopted in Fig. 4 for curves 2). It is seen from Fig. 7 a-b that for a "non-ideal" system the dispersion of threshold voltages brings about a fixed-pattern noise and a spread of currents integrated in the readouts, $I_{in}(V_G)$. For multi-element IR FPAs, with allowance for the spread of threshold voltages, at a voltage V_G =1.205 V (Fig.5b), for which the detectivity of a single channel D*

attains a maximum, the spread of currents I_{in} integrated in the readouts falls in the range from $4 \cdot 10^{-9}$ to $1.15 \cdot 10^{-8}$ A (Fig. 7a), whereas the current integrated in the "ideal" system is $I_{in} = 0.8 \cdot 10^{-8}$ A.

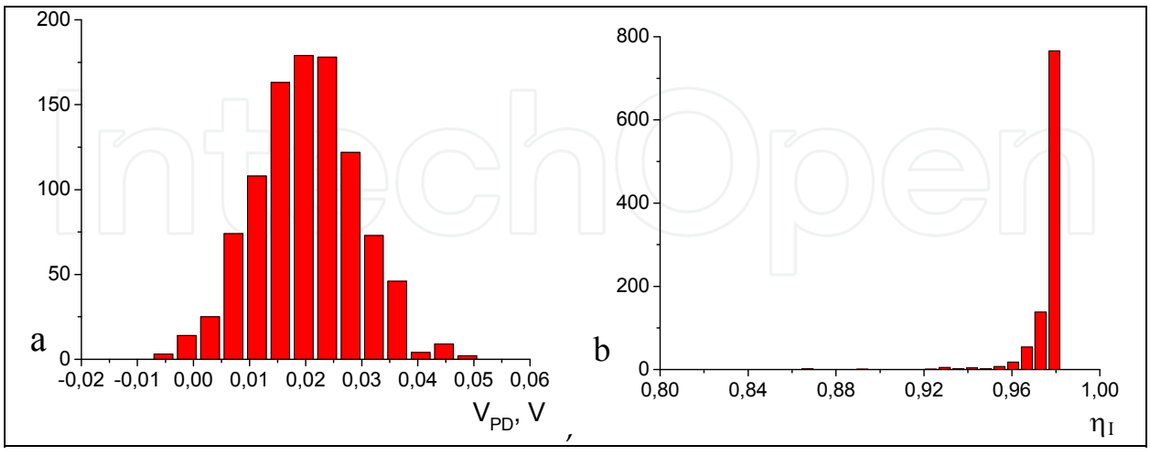

Fig. 6. Effect due to the spread of FET threshold voltages on the characteristics of multi-element IR FPAs; a – histogram of photodiode voltages, b – histogram of injection efficiencies η_I for $I_0=5 \cdot 10^{-10}$ A, $R_P = 3 \cdot 10^7$ Ohm, $I_P = 1 \cdot 10^{-8}$A, $\eta_K = 0.8$, and $V_G=1.225$ V. The standard deviation of input-FET threshold voltages is $\sigma(V_{th}) = 10$ mV.

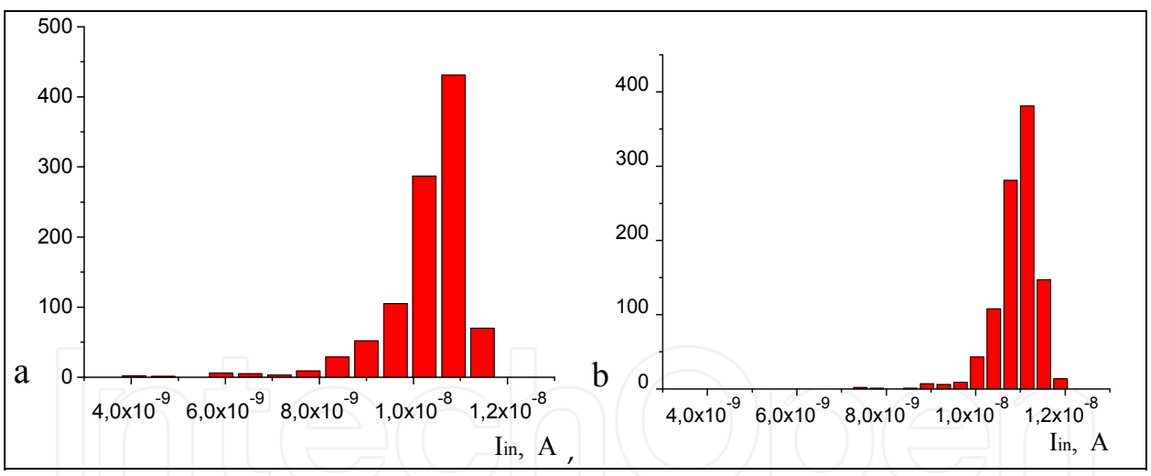

Fig. 7. Calculated histograms $I_{in}(V_G)$ for a normal distribution of input-FET threshold voltages with $\sigma(V_{th}) = 10$ mV. For Figs. 7a and 7b the voltages V_G are respectively 1.205 Vand 1.225 V. The calculations were performed for photodiodes with parameter values the same as those for curves 2 in Fig. 4.

Figure 8 show histograms $D^*(V_G)$ calculated with allowance for the spread of threshold voltages. In the calculations of detectivity, the accumulation time was defined by the charge capacity of the readout circuit and by the maximal (over 1000 realizations) current $I_{in}(V_G)$.

In multi-element IR FPAs, in view of non-uniformity of threshold voltages, at $V_G = 1.205$ V about 1% of photodetector channels have a detectivity D* lower than $1 \cdot 10^{11}$ cm $\cdot$Hz$^{1/2}$ $\cdot$Wt^{-1} (see Fig. 8b), whereas for a single channel we have $D^* = 2.48 \cdot 10^{11}$ cm $\cdot$Hz$^{1/2}$ $\cdot$Wt^{-1}. In the case

of multi-element IR FPAs because of the spread of threshold voltages, there arises a necessity to adjust the gate voltage (for the values of electrophysical parameters of photodiodes adopted in the calculations, Fig. 8b); the optimum value here is V_G =1.225 V. The increase of V_G results in a substantial reduction of fixed-pattern noise (see Fig.7b). In the latter situation, the minimal detectivity is not lower than $1.85 \cdot 10^{11}$ cm·Hz$^{1/2}$·Wt^{-1}, and more than 98% pixels have a detectivity D* greater than $2.0 \cdot 10^{11}$ cm·Hz$^{1/2}$·Wt^{-1}. With further increase of V_G, "dark" parasitic photodiode current components grow in value and the detectivity of the majority of photodetector channels decreases (Fig. 8c).

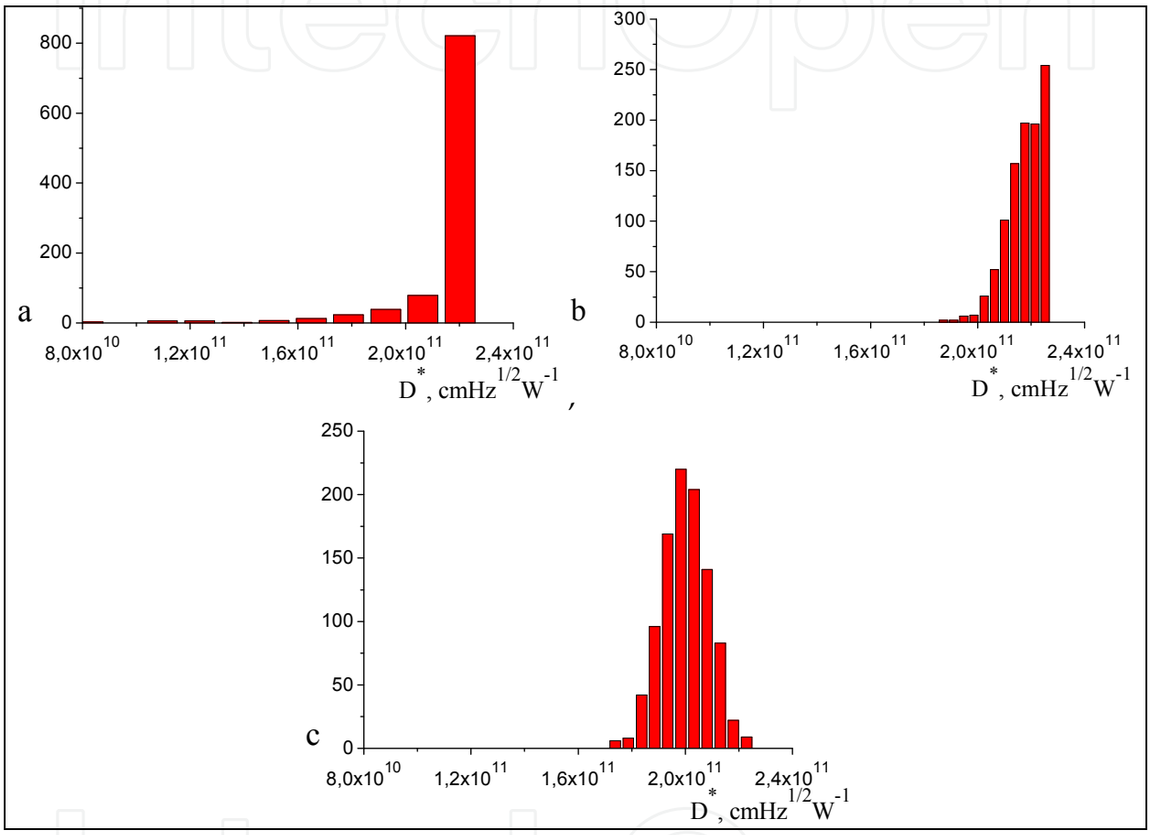

Fig. 8. Histograms D*(V_G) calculated for FET threshold voltages normally distributed with σ(V_{th}) = 10 mV for V_G = 1.201, 1.225, and 1.249 V (respectively Figs. 8a, 8b, and 8.6c). The calculations were performed for photodiodes with parameter values adopted for curves 2 in Fig. 4.

The effect due to dispersion of threshold voltages in fabricated readout circuits is illustrated by a comparison of calculated histograms $I_{in}(V_G)$ and D*(V_G) in Fig. 8 with histograms calculated for σ(V_{th}) = 2 mV, Fig. 9. As it is seen from the calculated dependences in Fig. 9, in the latter case the detectivity of the multi-element IR FPA is at the level of about 90% of D* of the single photodetector channel.

Along with non-uniformity of input-FET threshold voltages, the photoelectric parameters of photodiodes, η_K, R_{PD}, and I_0, also inevitably display some scatter of values. Figure 10 shows histograms of I_{in} (Fig. 10a) and D* (Fig.10b) calculated on the assumption that the distributions of R_{PD} and I_0 obey normal distribution laws.

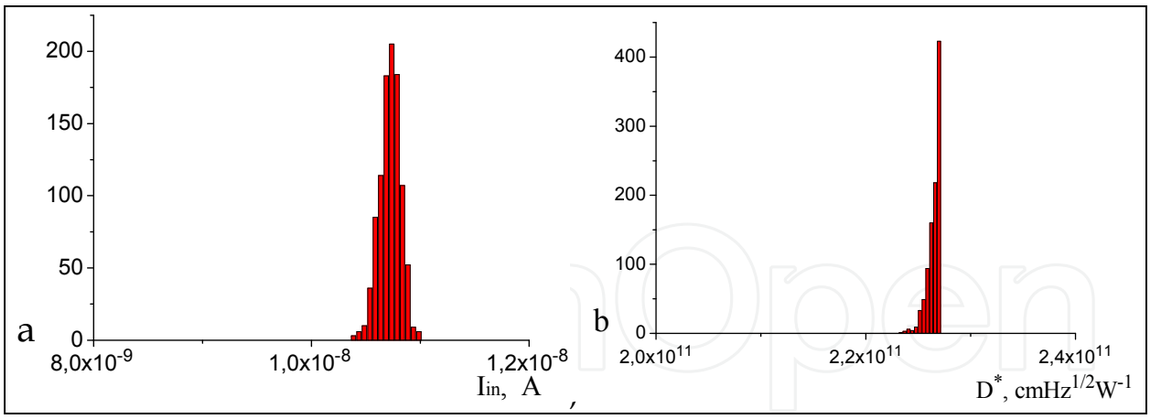

Fig. 9. Influence of the threshold voltage spread on the characteristics of multi-element IR FPAs; a – histogram of I_{in}, b – histogram of D*. The standard deviation of input-FET threshold voltages is $\sigma(V_{th})$ = 2 mV, I_0=5 ·10^{-10} A, R_{PD} =3 ·10^7 Ohm, I_P =1 ·10^{-8} A, η_K =0.8, V_G =1.213 V.

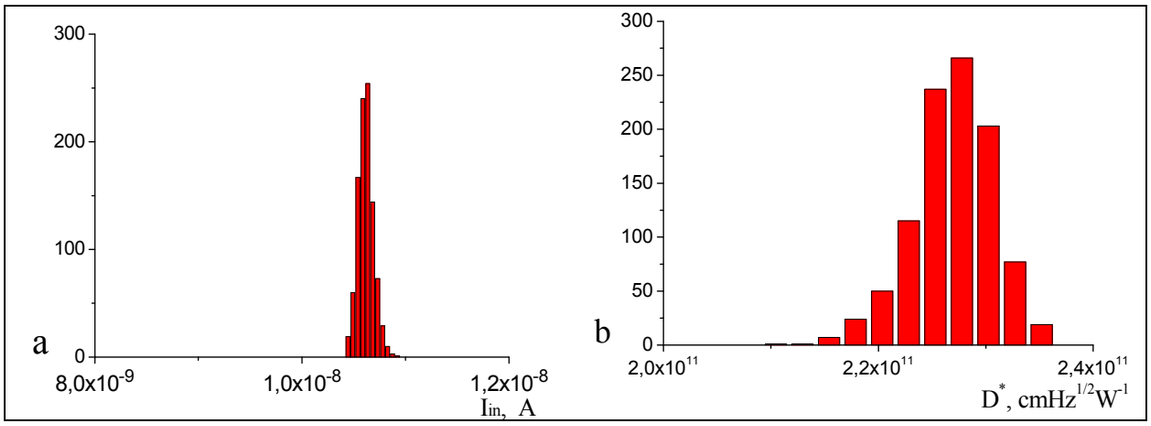

Fig. 10. Influence of the spread of photoelectric parameters of photodiodes on the performance characteristics of multi-element IR FPAs; a – histogram of I_{in}, b – histogram of D*. Parameter values adopted in the calculations: $\sigma(R_{PD})$ = 3 ·10^6 Ohm, $\sigma(I_0)$ = 1 ·10^{-10} A, I_0=5 ·10^{-10} A, R_{PD} =3 ·10^7 Ohm, I_P =1 ·10^{-8} A, η_K =0.8, V_G =1.225 V.

Plotting histograms of performance characteristics of multi-element IR FPAs, namely, currents integrated in the readout circuits and detectivity) versus the input-gate voltage V_G allows one to carry out numerical experiments and compare their results with experimental data. Such histograms can be considered generalized characteristics of multi-element IR FPAs indicative of their quality.

3.2 Modeling procedure for multi-element IR FPAs with direct injection readout circuits using the experimental-current voltage characteristics of photodiodes

The developed procedure enables performing an analysis of the system 'photodiode –direct-injection readout' using the experimental current-voltage characteristics of photodiodes. Figure 11 shows a family of "dark" and "light" current-voltage characteristics of one hundred photodiodes measured under room-temperature background conditions. The

photodiodes were fabricated on the basis of a $Hg_{1-x}Cd_xTe$ variband heteroepitaxial structure. The stoichiometric composition of the photosensitive layer was x=0.225 (Vasilyev, 2010).

In performing the calculations, the experimental current-voltage characteristics were approximated with the expressions:

$$I_{PD}(V_{PD}) = C_0 + C_1 \exp(C_2 V_{PD}) + C_3 \exp(C_4 V_{PD}) + C_5 V_{PD} \quad (11)$$

where the values of coefficients C_0-C_5 were chosen individually for each photodiode.

The characteristics of multi-element IR FPA were calculated by the procedure, described in section 3.1, that allows calculation of all photodetector-channel characteristics, $\eta_I(V_G)$, $I_{in}(V_G)$, and $D^*(V_G)$.

Figure 12 shows the histograms $D^*(V_G)$ and $I_{in}(V_G)$ calculated for the standard deviation value of threshold voltages of the readouts $\sigma(V_{th})$ =10 mV. An analysis of dependences calculated with lower values of $\sigma(V_{th})$ suggests that the use of silicon technology permitting values $\sigma(V_{th})$ < 2–3 mV will allow a substantial (by 20–30%) reduction of the fixed-pattern noise level. The changes in the calculated detectivity histograms proved to be less substantial since the spread of detectivity values is primarily defined by the variations of photodiode quantum efficiency (Vasilyev, 2010).

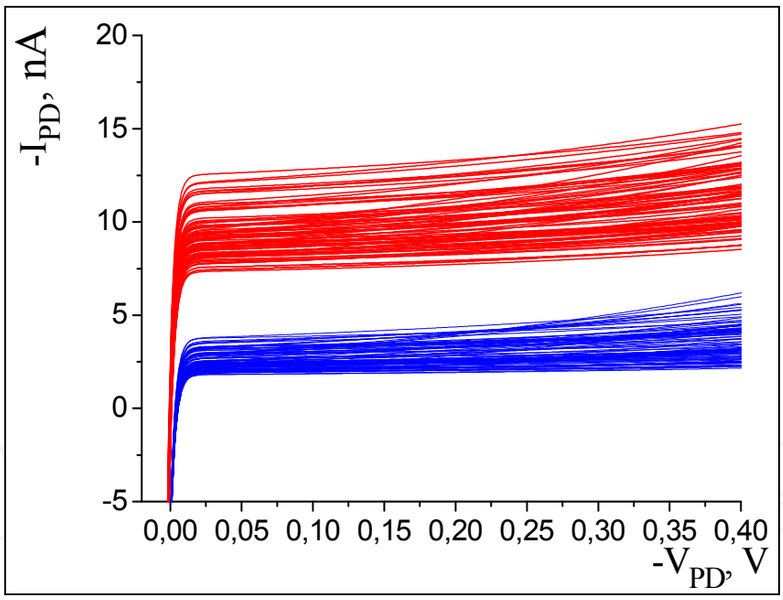

Fig. 11. A family of experimental current-voltage characteristics of $Hg_{1-x}Cd_xTe$ photodiodes; "dark" characteristics are shown with blue lines, and characteristics measured under room-temperature radiation background with red lines are shown with red lines.

It should be noted that the numerical values of coefficients α_1, α_2, α_3, and K were borrowed from literature sources. Experimentally measured values of these coefficients or more elaborated model for photodiode noises can easily be incorporated into the computer problem, allowing an improved accuracy in predicting the characteristics of IR FPAs.

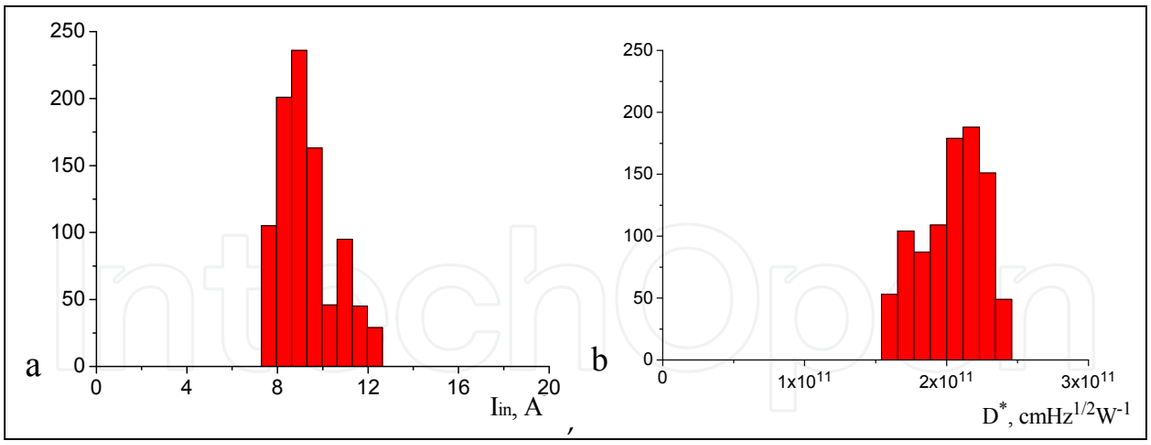

Fig. 12. Influence of the spread of photoelectric parameters of photodiodes on the performance characteristics of multi-element IR FPAs; a – histogram of I_{in}, b – histogram of D*. Parameter values adopted in the calculations: $\sigma(R_{PD})$ = 3 ·10^6 Ohm, $\sigma(I_0)$ = 1 ·10^{-10} A, I_0=5 ·10^{-10} A, R_{PD} =3 ·10^7 Ohm, I_P =1 ·10^{-8} A, η_K =0.8, V_G =1.225 V.

3.3 Analysis of LWIR thermography systems based on $Hg_{1-x}Cd_xTe$ photodiodes

The simple photodiode model (10) proved to be insufficient for adequately predicting the current-voltage characteristics of $Hg_{1-x}Cd_xTe$ photodiodes in the spectral region 8 to 14 μm. In modeling current-voltage characteristics of $Hg_{1-x}Cd_xTe$ photodiodes, all main mechanisms of charge transport in *p-n* junctions must be taken into account, including the background radiation current $\eta_K I_P$, the diffusion current, the thermal generation/recombination current, the tunneling current through localized levels within the bandgap of the depleted region of the *p-n* junction, the interband tunneling current (Anderson,1981), the Shockley-Reed-Hall current through traps in quasi-neutral *n* and *p* regions, the Auger current, and the radiative generation/recombination current in the *p-n* junction and in the quasi-neutral regions (Anderson, 1981; Rogalski, 2000). All the currents listed above are independent currents to be taken into account additively, except for the thermal generation-recombination and trap-assisted tunneling through traps of the Shockley-Reed-Hall type in the depleted region of the *p-n* junction, since the rates of the latter processes is determined by the trap occupation. The two latter mechanisms were modeled in the approximation of balance equations for charge carriers at trap levels (Anderson, 1981; Gumenjuk-Sichevska, 1999; Sizov, 2006; Yoshino,1999). We assumed the presence of localized donor-type centers in the bandgap with energy E_t=0.6-0.7E_g over the valence-band edge (Krishnamurthy, 2006). In calculating the band-gap energy of the material as a function of stoichiometric composition and temperature, we used the expression (Rogalski, 2000).

$$E(x,T)=\left[-0.302+x\left[1.93+x\left(-0.81+0.832x\right)\right]+5.32\cdot10^{-4}\cdot\left(1-2x\right)\frac{-1822.0+T^3}{255.2+T^2}\right] \quad (12)$$

The main electrophysical parameters of $Hg_{1-x}Cd_xTe$ photodiodes adopted in the calculation of their current-voltage characteristics are listed in Table 2.

By way of example, Figure 13 shows the current-voltage characteristics of $Hg_{1-x}Cd_xTe$ photodiodes for different long-wave spectral-response cutoffs, and Figure 14 shows the calculated dependences of R_{PD} A_{PD} on the cutoff wavelength of the spectral response of the photodiodes.

As it was shown in (Gumenjuk-Sichevska, 1999; Sizov, 2006), the photodiode model that was used in the present calculations permits calculation of the current-voltage characteristics as a function of the stoichiometric composition of $Hg_{1-x}Cd_xTe$, temperature, and electrophysical parameters of substrate material, the obtained dependences being consistent with those reported in the literature (Rogalski, 2000; Yoshino,1999).

Figure 15 shows the calculated dependences of the maximum values of $D^*(V_G)$ of a photodetector channel based on the system 'HgCdTe photodiode – direct injection readout circuit' on the cutoff wavelength λ_2. In calculating the background radiation flux reaching the photodiodes in the spectral region from λ_1 to λ_2 (λ_1 =4 μm and λ_2 is the cutoff wavelength), for the blackbody temperature a value 300 K was adopted; the aperture angle was assumed defined by the relative aperture of the optical system F/f = 0.5, and for the transmission of the optical system, a value 0.9 was adopted.

Designation	Parameter	Numerical value	
		Case 1	Case 2
N_a, N_d	Acceptor and donor concentrations	$1.0 \cdot 10^{22}$ m^{-3}, $2.0 \cdot 10^{21}$ m^{-3}	$2.0 \cdot 10^{22}$ m^{-3}, $2.0 \cdot 10^{21}$ m^{-3}
N_t, N_{tV}	Concentration of traps in the p-n junction and in the quasi-neutral regions	$6.0 \cdot 10^{21}$ m^{-3}, $2.0 \cdot 10^{21}$ m^{-3}	$3.0 \cdot 10^{21}$ m^{-3}, $1.0 \cdot 10^{21}$ m^{-3}
τ_n, τ_p, τ_{nV}, τ_{pV}	Electron and hole lifetimes in the p-n junction and in the quasi-neutral regions	$0.2 \cdot 10^{-6}$ s, $0.2 \cdot 10^{-6}$ s, $6.0 \cdot 10^{-6}$ s, $6.0 \cdot 10^{-6}$ s	$0.2 \cdot 10^{-6}$ s, $0.2 \cdot 10^{-6}$ s, $1.0 \cdot 10^{-7}$ s, $1.0 \cdot 10^{-7}$ s
E_t	Energy position of trap level	E_t=0.7 E_g eV	
P	Interband matrix element	$8.3 \cdot 10^{-10}$ eV·m	
W_c^2	Squared matrix element for the tunneling of charge carriers from the trap level into the band	$3 \cdot 10^{-67}$ J^2·m^3	
Δ	Spin – orbital interaction constant	0.96 eV	
ε_r	Static dielectric permittivity	17.5	
A_{PD}	Photodiode area	$9 \cdot 10^{-5}$ cm^2	

Table 2. Electrophysical parameters of $Hg_{1-x}Cd_xTe$ photodiodes.

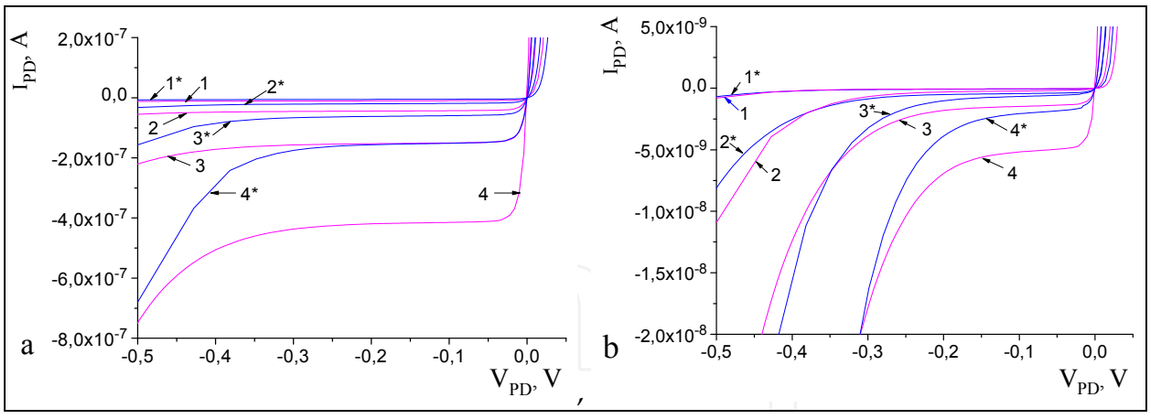

Fig. 13. Calculated current-voltage characteristics of $Hg_{1-x}Cd_xTe$ photodiodes at temperatures 77 K (a) and 60 K (b). For curves 1 – 4 (1* - 4*) the cutoff wavelength is respectively λ_2 = 11, 12, 13, and 14 μm. The electrophysical parameters of photodiodes are listed in Table 2; case 1 – curves 1-4, case 2 - curves 1* - 4*.

The detectivity of the photodetector channel at temperature T=77 K for photodiodes with electrophysical-parameter values indicated as case 1 in Table 2 (curve 1 in Fig. 15) at $\lambda_2 > 10$ μm becomes lower than Background Limited Performance (BLIP) detectivity (curve 3). On cooling the photodiodes to temperature 60 K, the detectivity of photodetector channel approaches BLIP detectivity at wavelengths below ~ 13 μm (curve 3). For photodiodes with electrophysical-parameter values indicated as case 2 in Table 2.2, due to a larger dynamic resistance, the long-wave spectral-response cutoff at which the FPA detectivity attains its maximum value shifts towards longer wavelengths (see curves 2 and 4 in Fig. 15).

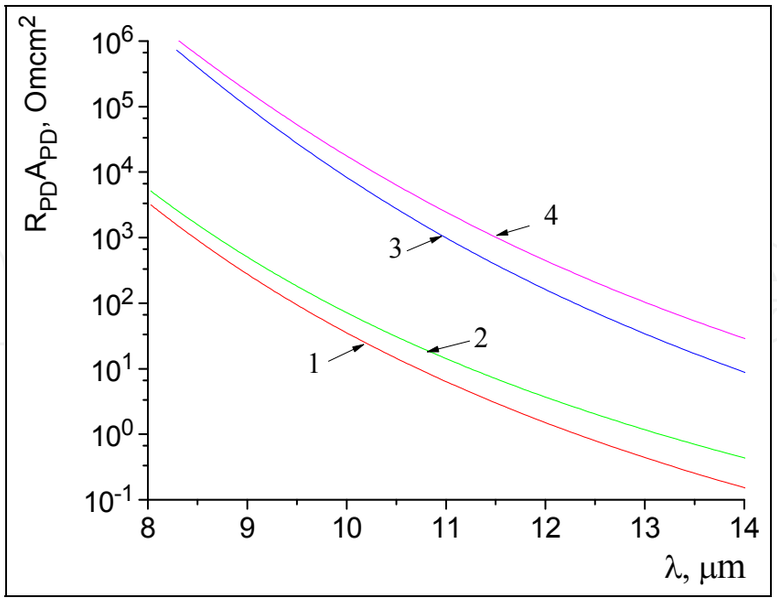

Fig. 14. Calculated dependences of R_{PD} A_{PD} on the long-wave cutoff of photodiodes; curves 1 and 2 refer to temperature T=77 K, and curves 3 and 4, to temperature T=60 K. Electrophysical-parameter values: curves 1 and 3 – case 1, curves 2 and 4 – case 2.

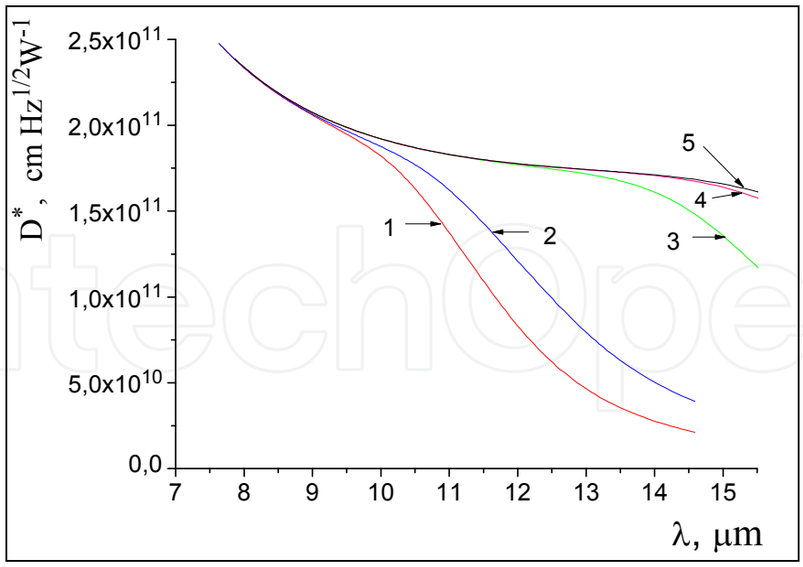

Fig. 15. Calculated curves $D^*(\lambda_2)$ for a photodetector channel based on the system '$Hg_{1-x}Cd_xTe$ photodiode-direct injection readout'; 1, 2 – photodiode temperature 77 K, 3, 4 – photodiode temperature 60 K. Curves 1, 3 and 2, 4 were calculated for parameter values indicated in Table 1 as cases 1 and 2, respectively, for direct injection charge capacity $Q_{in}=5\cdot10^7$ electrons. Curve 5 – calculated dependences for BLIP detectivity.

Figure 16 shows the curves $D^*(V_G)$ and the dependences $Q_1(V_G)$, $Q_2(V_G)$, $Q_3(V_G)$, $Q_4(V_G)$ and $Q_5(V_G)$ calculated for λ_2 = 10, 12, and 13 μm. The calculations were performed for photodiodes with parameter values indicated in Table 2 as case 1.

The detectivity of the photodetector channel (Fig. 16a) at λ_2 = 10 μm is close to BLIP detectivity D^*; this detectivity is limited by the photodiode current noise Q_3 and at voltages V_G >1.2 V it is almost independent of V_G. For λ_2 = 12 μm (Fig. 16b) the maximum detectivity of the photodetector channel is $D^* \approx 8.34\cdot10^{10}$ cm·Hz$^{1/2}$·Wt^{-1} (BLIP detectivity is $D^*= 1.77\cdot10^{11}$ cm·Hz$^{1/2}$·Wt^{-1}). For λ_2 = 13 μm (Fig. 16c) the maximum detectivity of the photodetector channel is $D^* \approx 4.7\cdot10^{10}$ cm·Hz$^{1/2}$·Wt^{-1} (BLIP detectivity is $D^*= 1.74\cdot10^{11}$ cm·Hz$^{1/2}$·Wt^{-1}). The degradation of detectivity at voltages V_G > 1.225 V is primarily defined by the increase in the photodiode 1/f-noise level (Q_4 in Fig. 16b, c).

An increase of the direct injection storage capacitance and the related increase of the accumulation time both lead to a greater contribution made by the 1/f-noise. Figure 17 shows the curves $D^*(V_G)$ and the dependences $Q_1(V_G)$, $Q_2(V_G)$, $Q_3(V_G)$, and $Q_4(V_G)$ similar to those shown in Fig. 16b yet calculated for direct injection storage capacity $Q_{in} = 2\cdot10^8$ electrons.

A comparison between the dependences in Figs. 16 and 17 shows that the maximal detectivity rather weakly depends on the storage capacity of the readout circuit. Yet, because of the increased contribution due to the 1/f noise of photodiodes, with increasing the input-gate voltage the dependence of D^* on V_G becomes more clearly manifested. That is why with increasing the storage capacity of direct injection readouts and, hence, with increasing the accumulation time, the requirements imposed on the standard deviation of threshold voltages become more stringent.

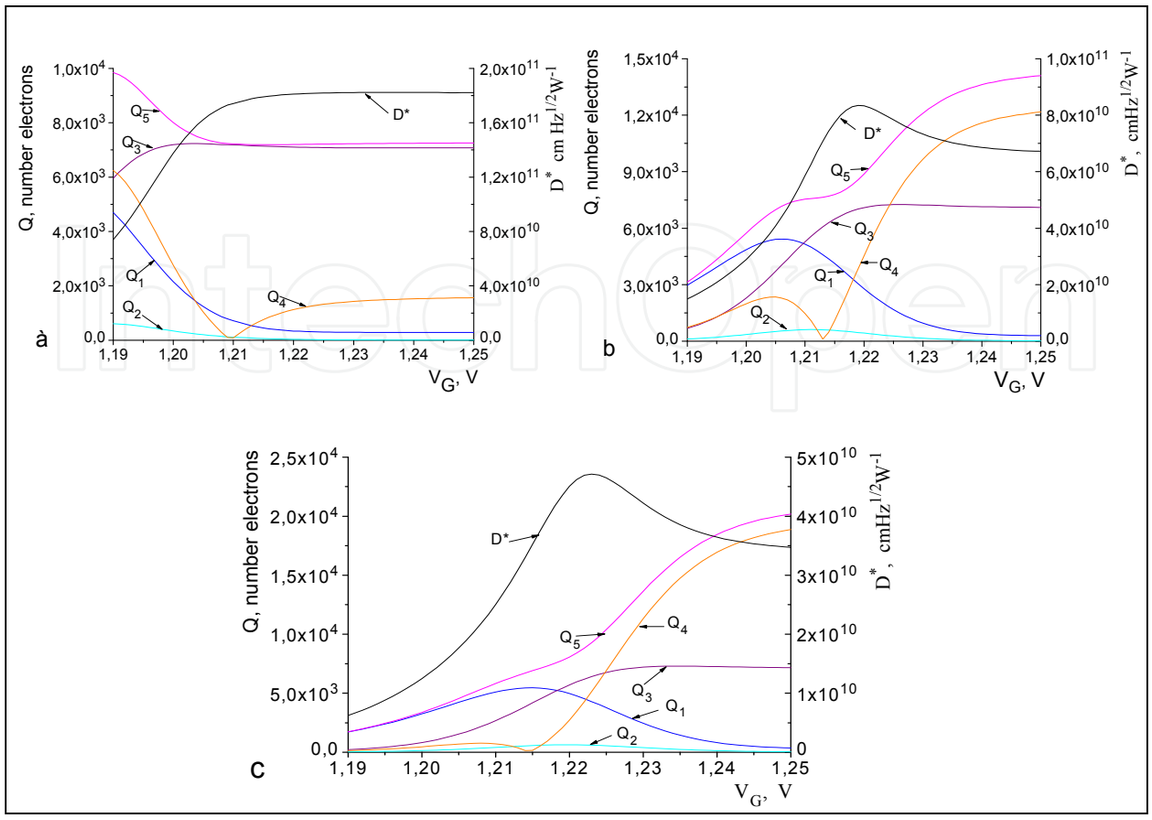

Fig. 16. Curves $D^*(V_G)$ (right axis) and dependences $Q_1(V_G)$, $Q_2(V_G)$, $Q_3(V_G)$, $Q_4(V_G)$, and $Q_5(V_G)$ (left axis). Temperature 77 K, direct injection charge capacity $Q_{in}=5 \cdot 10^7$ electrons; a – λ_2 =10 μm, b – λ_2 = 12 μm, c – λ_2 = 13 μm.

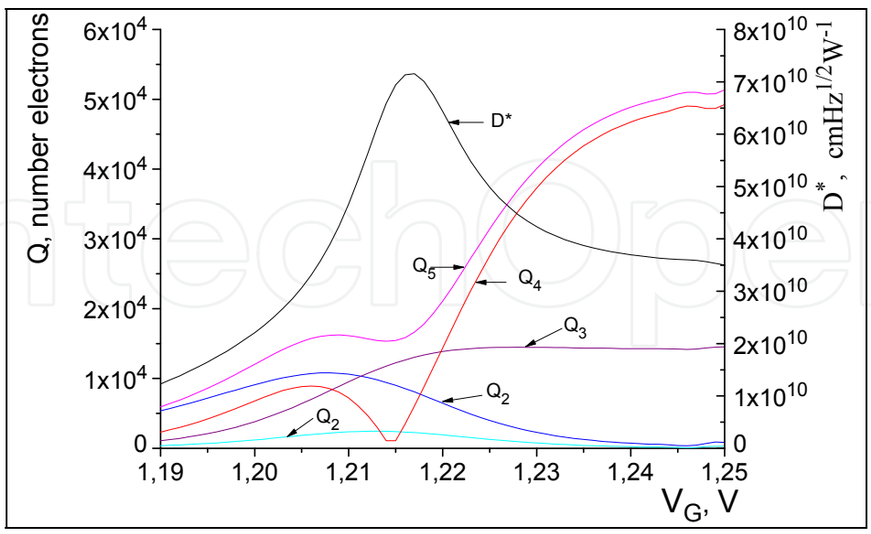

Fig. 17. Calculated curves $D^*(V_G)$ (right axis) and dependences $Q_1(V_G)$, $Q_2(V_G)$, $Q_3(V_G)$, $Q_4(V_G)$, and $Q_5(V_G)$ (left axis). The photodiode temperature is 77 K; the storage capacity of direct injection readout is $Q_{in}=2 \cdot 10^8$ electrons; λ_2 = 12 μm. The values of electrophysical parameters of photodiodes are given in Table 2.2, case 1.

4. Temperature resolution of thermography systems based on multi-element IR FPAs with direct injection readouts

For thermography systems based on multi-element photodetectors, an important figure of merit is the noise-equivalent temperature difference (NETD) (Rogalski, 2000). The NEDT value can be calculated by the formula (Taubkin, 1993).

$$\mathrm{NETD} = \frac{\sqrt{1/2\mathrm{T_{in}}}}{\frac{\mathrm{F}^2}{4\mathrm{f}^2}\left(\mathrm{A_{PD}}\right)^{1/2}\mathrm{G_{Op}}\int_{\lambda 1}^{\lambda 2}\frac{\mathrm{d}\left(\mathrm{dR}/\mathrm{d}\lambda\right)}{\mathrm{dT}}\mathrm{S}(\lambda)\mathrm{D}^*_\lambda\left(\lambda_1,\lambda_2,\mathrm{T}\right)\mathrm{d}\lambda} \tag{13}$$

Here, $dR/d\lambda$ is the blackbody spectral luminous exitance, F/f is the relative aperture of the optical system, f is the focal distance, G_{Op} is the optical transmission of the system, and $S(\lambda)$ is the atmospheric transmission.

An analysis of NETD starts with calculating the current-voltage characteristics of photodiodes and the background radiation level. Then, currents integrated in the readout circuit and detectivity are calculated.

Figure 18 shows the calculated curves of NETD versus the cutoff wavelength λ_2.

For an "ideal" thermography system (curve 1), in which the integration time is equal to the frame time, T_{in} =20 ms in the present calculations, and the detectivity of photodetector channels is close to BLIP detectivity, we obtain the well-known dependences NETD(λ) that show that the temperature resolution improves with increasing the wavelength λ_2. The dependencies in Fig. 18 reveal the causes of the losses in temperature resolution owing to insufficiently high dynamic resistance of photodiodes or limited storage capacitance of silicon direct injection readout circuits of thermography systems in comparison with the theoretical limit. It can be inferred from the dependences $D_\lambda^*(\lambda_2)$ (Fig. 15) and NETD(λ_2) (Fig. 18) that the temperature resolution of thermography systems based on the photodiode – direct injection readout system attains a maximum value at some wavelength λ_2 and, then, decreases (see curves 2 and 3 in Fig. 18). The position of NEDT maximum is defined by electrophysical parameters of HgCdTe photodiodes, by the optical transmission of the system, and by the photodiode temperature. Yet, as it follows from the calculated curves of NETD in Fig. 18 (curves 4-7) the main factor limiting the temperature resolution of the thermography systems is the storage capacitance of silicon readout circuits.

With increasing the cutoff wavelength λ_2, the intensity of background radiation coming to photodetector also increases and, as a result, the integration time T_H decreases, with simultaneous shift of the maximum temperature resolution of the thermography system towards short wavelengths in comparison with curves 2 and 3 in Fig. 18. The charge capacity of readout circuits Q_{in} = $5 \cdot 10^7$ electrons presents a maximal value reported in literature for multi-element matrix IR FPAs (at 30-μm photocell pitch) (Rogalski, 2000). At such values of integration capacitance of readout circuits the temperature resolution of thermography systems (curve 5) already with λ_2 = 8 μm is more than one order of magnitude and with λ_2 = 14 μm, two orders of magnitude lower than that of the "ideal" thermography system (curve 1). The storage capacitance can be increased through implementing a new architecture of readout circuits (curves 6 and 7 in Fig. 18) (Lee, 2010). A

cardinal solution here is implementation of ADC in each pixel of the readout circuit (Zhou, 1996; Martijn, 2000; Fowler, 2000). In (Bisotto, 2010), each pixel was provided with a 15-bit ADC, and the effective storage capacitance was in excess of $3 \cdot 10^9$ electrons. This has enabled an increase in integration time up to the frame time and, in this way, allowed reaching a NETD of LWIR thermography systems based on multi-element IR FPAs amounting to 2 mK, the latter value being close to the maximum theoretically possible NETD.

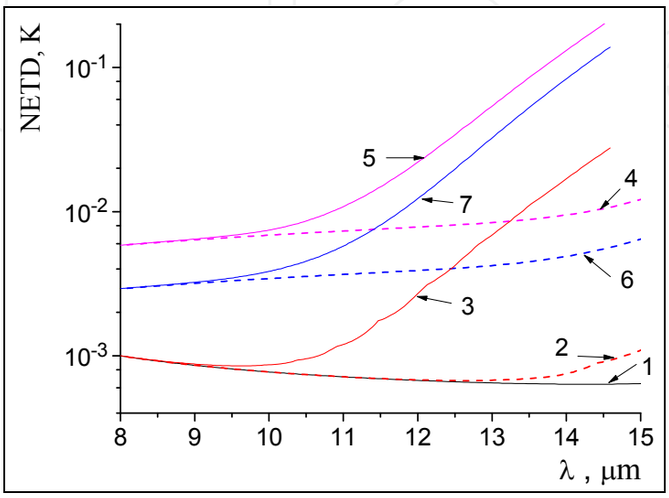

Fig. 18. Calculated curves NETD(λ_2). In the calculations, the values F_p/f= 0.5 and λ_1 =5 μm were adopted. Curve 1 was calculated for $D^*_\lambda = D^*_{\lambda BLIP}$ and $T_н$=20 ms; curves 2 and 3 were calculated with allowance for the dependence of D^*_λ on the long-wave spectral-response cutoff, integration time T_{in}=20 ms; curves 4-7 were calculated for conditions with limited storage capacitance of direct injection readouts (curves 4 and 5 - $Q_{in} = 5 \cdot 10^7$ electrons, curves 6 and 7 - $Q_{in} = 2 \cdot 10^8$ electrons); curves 2, 4, and 6 – photodiode temperature 60 K, curves 3, 5, and 7 – photodiode temperature 77 K. The electrophysical parameters of photodiodes are given in Table 2, case 1.

The dependences $D^*(V_G)$ and NETD(λ_2) calculated for different values of the storage capacity of readout circuits on the input-gate voltage V_G and shown in Figs. 15-18 define the ultimate performance characteristics of thermography systems in the spectral range 8-14 μm. In fact, these dependences are will also be observed for a single-element FPA based on the system 'Hg$_{1-x}$Cd$_x$Te photodiode – direct injection readout circuit' since they were plotted using just the maximum values of D^*. For multi-element IR FPAs, the non-uniformity of input-FET threshold voltages leads to an increased fixed-pattern noise level and, for some part of photodetector channels, to a considerable reduction of D^* and NETD in comparison with the dependences shown in Figs. 15 and 18. An additional factor causing an increase in the fixed-pattern noise, a decrease of detectivity, and worsened temperature resolution of multi-element IR FPAs is non-uniformity of the stoichiometric composition of the Hg$_{1-x}$Cd$_x$Te substrate.

For multi-element IR FPAs with $\lambda_2 \leq 10$ μm, detectivity rather weakly depends on the gate voltage V_G and, hence, on the dispersion of threshold voltages (see Fig.16a). The fixed-pattern noise level and the spread of NETD values of multi-channel IR FPAs are primarily defined by the scatter of the long-wave photosensitivity cutoff owing to non-uniform stoichiometric composition of the Hg$_{1-x}$Cd$_x$Te substrate.

Figure 19 shows calculated histograms of D*, I_{in} and NETD values of thermography systems for $Hg_{1-x}Cd_xTe$ photodiodes with photoelectric parameters given in Table 2, case 1. In the calculations, it was assumed that the dispersion of threshold voltages and the non-uniformity of the stoichiometric composition of substrate material obey normal distribution laws with parameter values indicated in the caption to the figure (the total number of realizations in the calculations was 200).

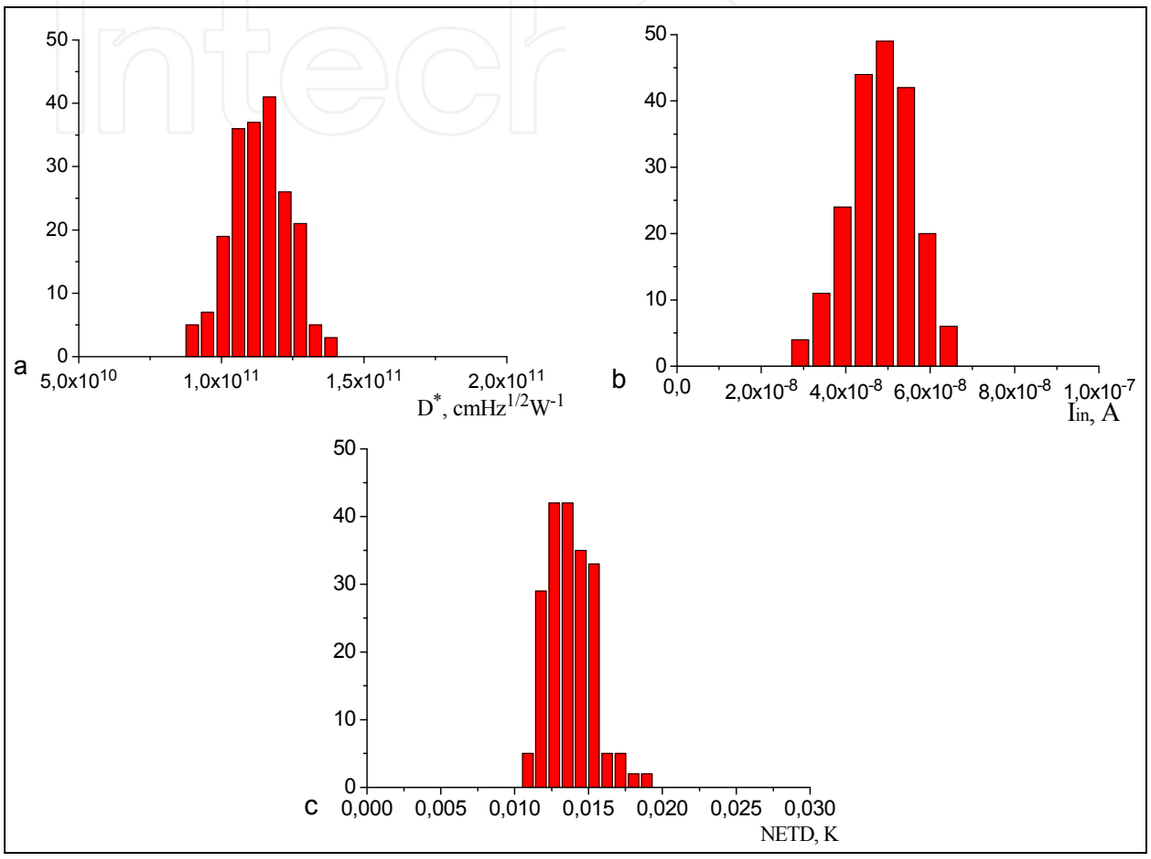

Fig. 19. Calculated histograms of performance characteristics of multi-element IR FPAs; a - detectivity D*, b – currents I_{in} integrated in the readout circuits, c - NETD. Standard deviation of input-FET threshold voltages - $\sigma(V_{th})$=5 mV. Standard deviation of the stoichiometric composition of $Hg_{1-x}Cd_xTe$ substrate - $\sigma(x)$ = 0.1%. Average stoichiometric composition - x=0.2167, T=77 K, storage capacitance of readout circuit $Q_{in}=5 \cdot 10^7$ electrons.

The photocurrent level was calculated with allowance for the long-wave cutoff of photosensitivity individually for each photodiode. The integration time was defined by the magnitude of the storage capacitance of the readout circuit and by the maximum level of photodiode current over 200 realizations. At T=77 K, the mean stoichiometric composition x=0.2167 ensures a long-wave photosensitivity cutoff λ_2=11 μm at standard dispersion of stoichiometric composition $\sigma(x)$ = 0.1%, typical of the present-day state-of-the-art technology level (Rogalski, 2000).

For a single channel with c λ_2=11 μm, at the same values of electrophysical and design parameters of photodiodes and readout circuits the maximum sensitivity D* is $1.4 \cdot 10^{11}$

cm·Hz$^{1/2}$·W^{-1}, D_{BLIP}* =1.8·10^{11} cm·Hz$^{1/2}$·W^{-1}, and NETD=10.8 mK (see curve 5 in Fig. 18). The dispersion of the stoichiometric composition of substrate σ(x) = 0.1% results in a spread of long-wave cutoff wavelengths in the interval from 11 to 11.8 μm, this being the main factor causing NETD degradation.

With increasing the long-wave cutoff wavelength λ_2, requirements to the uniformity of threshold voltages under the input gates of direct injection readout circuits and requirements to the uniformity of the stoichiometric composition of substrate both become more stringent. Figure 20 shows calculated histograms of currents I_{in}, detectivities D* and NETD values of thermography systems for $Hg_{1-x}Cd_xTe$ photodiodes with photoelectric parameters indicated in Table 2 as case 1. At mean stoichiometric composition x=0.21055, σ(x) = 0.1% and T=77 K the non-uniformity of the stoichiometric composition of substrate material results in a spread of long-wave photosensitivity cutoffs in the interval from 12 to 13.2 μm. The input-gate voltage value V_G=1.23 V appears to be optimal for the radiation environment conditions and values of electrophysical and design parameters of photodiodes and readout circuits adopted in the calculations.

Note that for a single channel at λ_2=12 μm the maximum detectivity D* is 8.4·10^{10} cm·Hz$^{1/2}$·W^{-1} and NETD = 0.022 K (Fig. 18, curve 5). Taking the dispersion of threshold voltages with σ(V_{th}) = 5 mV and substrate stoichiometric composition with σ(x) = 0.1% into account results to two-three-fold degradation of NETD in a considerable fraction of photodetector channels.

Figure 21 shows calculated histograms of currents I_{in}, detectivities D* and NETD values of thermography systems for $Hg_{1-x}Cd_xTe$ photodiodes with photoelectric-parameter values adopted in Fig. 20 yet under more stringent conditions in terms of the dispersion of FET threshold voltages and stoichiometric composition of $Hg_{1-x}Cd_xTe$ substrate, σ(V_{th}) = 2 mV and σ(x) = 0.03%. A comparison between the histograms in Figs. 20 and 21 shows that more stringent requirements imposed on the uniformity of threshold voltages and stoichiometric composition of substrate allow a substantial reduction of the fixed-pattern noise and a considerable improvement of NEDT values of thermography systems.

With the adopted values of electrophysical parameters of Si readout circuits and $Hg_{1-x}Cd_xTe$ photodiodes (Tables 1 and 2), thermography systems based on multi-element IR FPAs intended for operation at liquid-nitrogen temperature in the spectral range up to 13-14 μm with maximum possible NETD values (Fig. 18, curve 5) can be implemented at an acceptable level of fixed-pattern noise by:

- increasing the dynamic resistance of $Hg_{1-x}Cd_xTe$ photodiodes;
- adhering to more stringent requirements in terms of uniformity of input-FET threshold voltages and stoichiometric-composition uniformity of the substrate.

However, requirements to σ(V_{th}) and σ(x) more stringent than the requirements that were adopted in calculating data in Fig. 21 presently cannot be met by silicon CMOS technology and synthesis processes of epitaxial $Hg_{1-x}Cd_xTe$ layers (Phillips, 2002).

Achieving photosensitivity in the spectral region 12-14 μm necessitates cooling the hybrid IR FPA assembly to a temperature below liquid-nitrogen temperature, see curves 4 and 6 in Fig. 19.

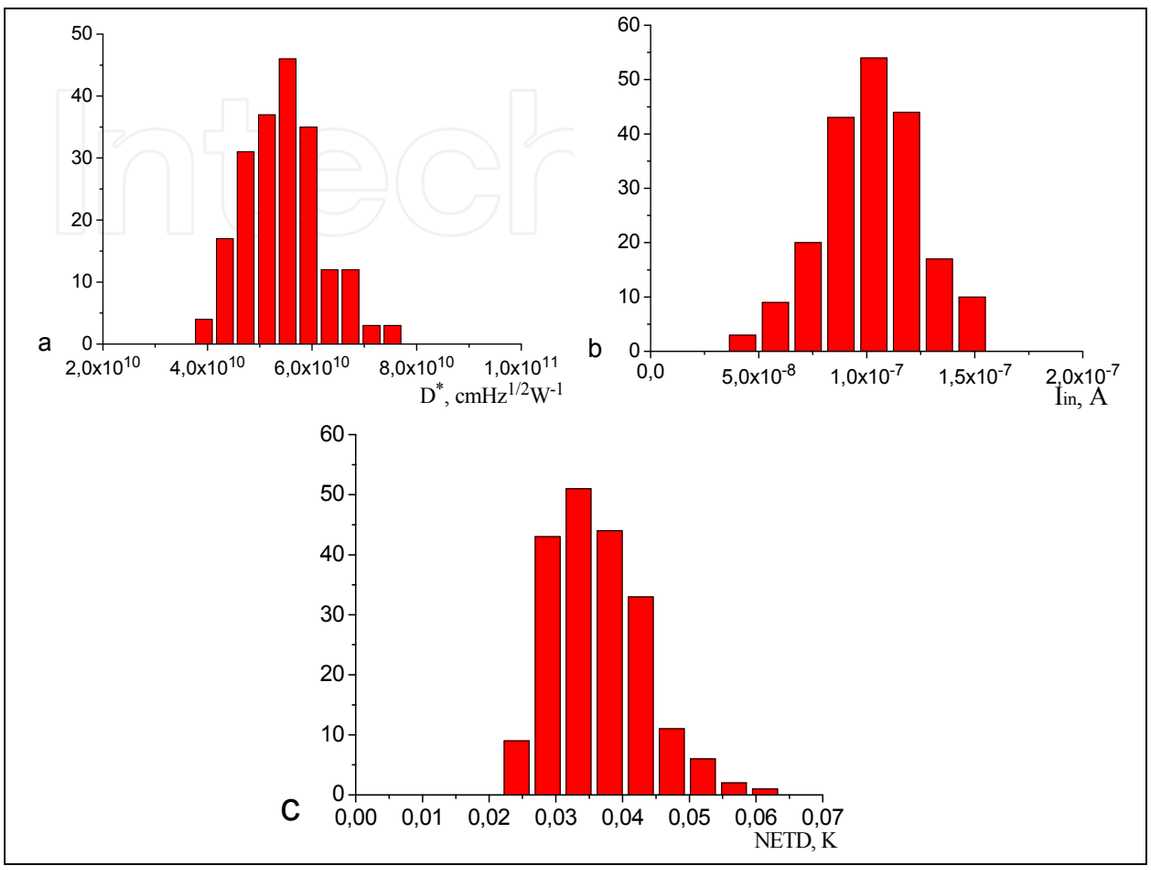

Fig. 20. Calculated histograms of performance characteristics of multi-element IR FPAs; a - detectivity D*, b – currents I_{in} integrated in the readout circuits, c - NETD. Standard deviation of input-FET threshold voltages - $\sigma(V_{th})$ = 5 mV. Standard deviation of the stoichiometric composition of $Hg_{1-x}Cd_xTe$ substrate $\sigma(x)$ = 0.1%. Average stoichiometric composition x=0.2105, T=77 K. Storage capacitance of readout circuit - $Q_{in}=5 \cdot 10^7$ electrons.

Figure 22 shows calculated histograms of currents detectivities D*, I_{in} and NETD values of thermography systems for $Hg_{1-x}Cd_xTe$ photodiodes with photoelectric parameters indicated in Table 2 as case 1. The parameter values used in the calculations were the same as those in Figs. 19 and 20, and the photodiode temperature was assumed to be 60 K.

At mean stoichiometric composition x=0.2105, 0.1% dispersion of stoichiometric composition and temperature T=60 K, the long cutoff wavelength will fall into the wavelength interval from 12.6 to 14 μm.

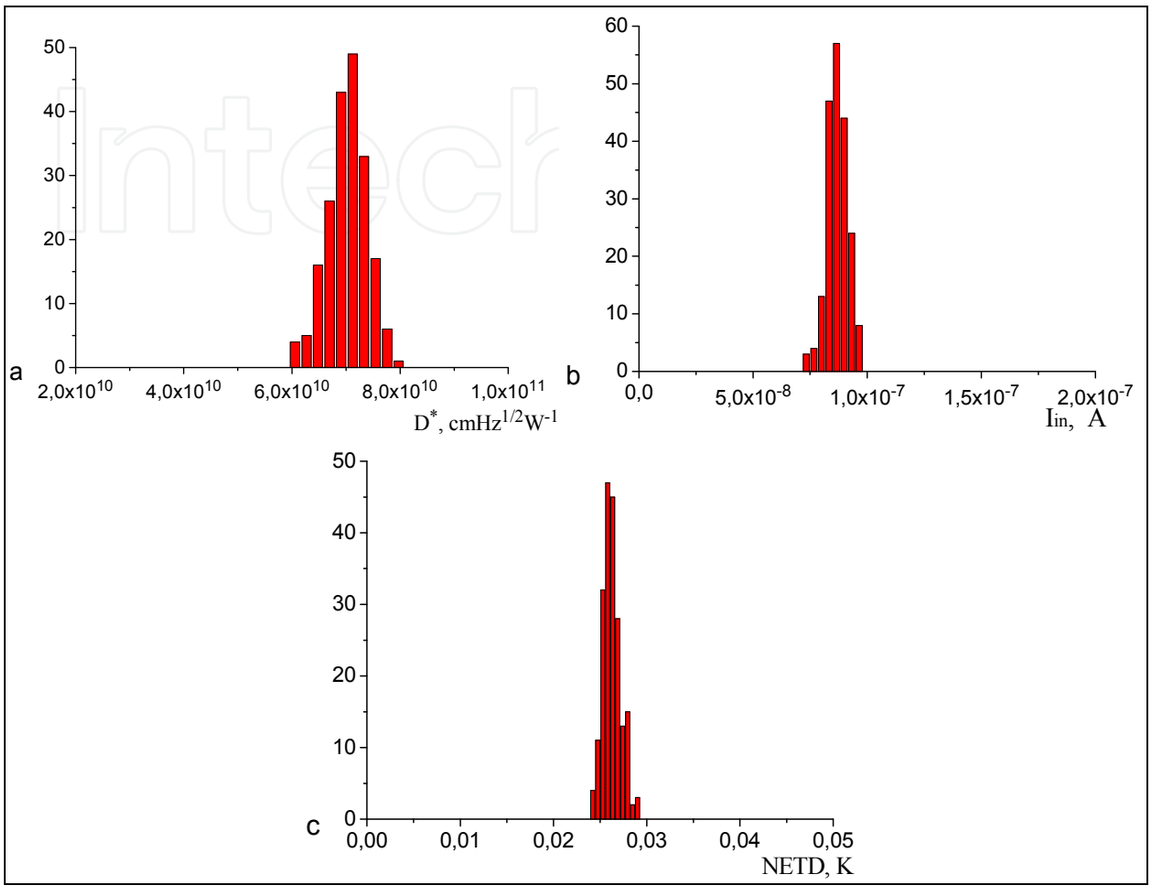

Fig. 21. Calculated histograms of performance characteristics of multi-element IR FPAs; a - detectivity D*, b – currents I_{in} integrated in the readout circuits, c - NETD. Standard deviation of input-FET threshold voltages - $\sigma(V_{th})$ = 2 mV. Standard deviation of the stoichiometric composition of $Hg_{1-x}Cd_xTe$ substrate $\sigma(x)$ = 0.03%. Average stoichiometric composition x=0.2126, T=77 K.

As it follows from the calculated dependencies shown in Fig. 22, the cooling of the hybrid assembly down to temperature 60 K will allow implementation of thermography systems with NEDT values close to maximum possible figures, limited only by the value of the storage capacitance of silicon readout circuits at an acceptable level of fixed-pattern noise. The possibility of variation of the cooling temperature of hybrid assembly in the calculations allows formulation of requirements to required accuracy in maintaining the temperature of cooled hybrid assembly, i.e. requirements to be imposed on the cryostat and cooling system.

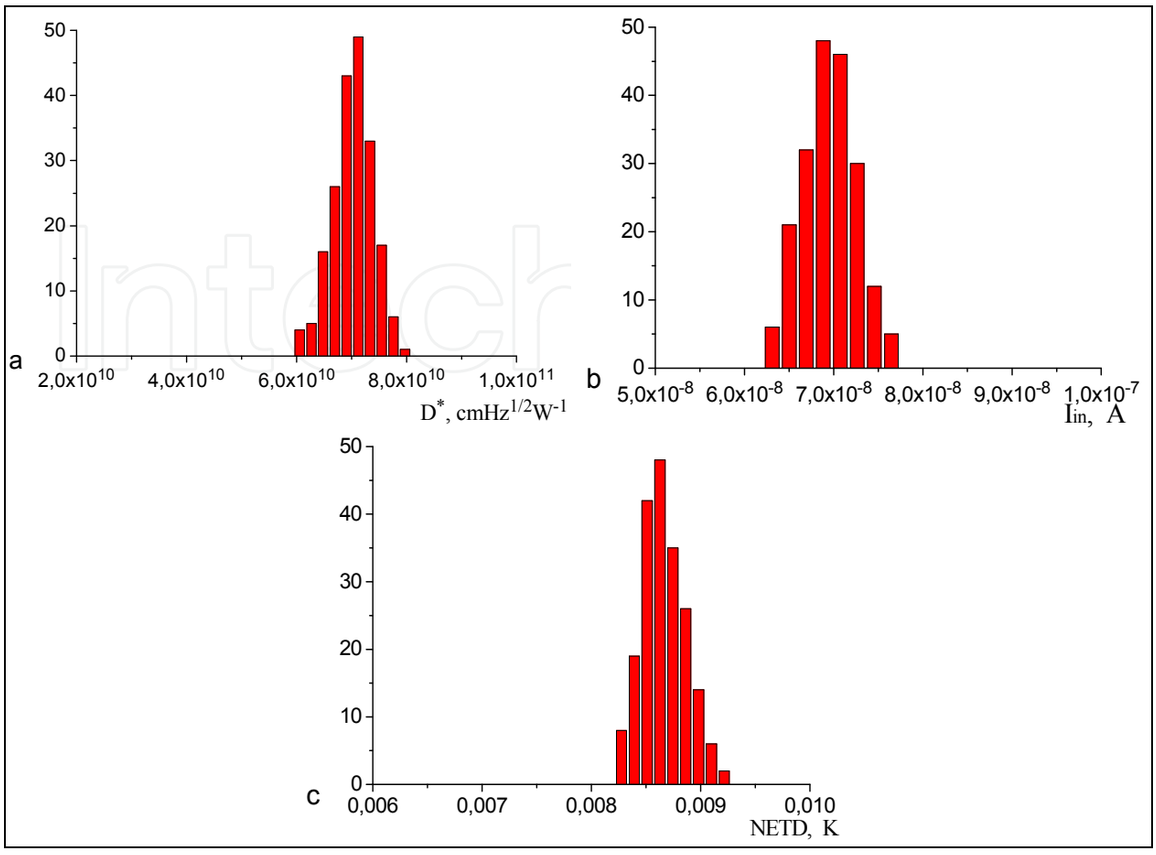

Fig. 22. Calculated histograms of performance characteristics of multi-element IR FPAs; a - detectivity D*, b – currents I_{in} integrated in the readout circuits, c - NETD. Standard deviation of input-FET threshold voltages - $\sigma(V_{th})$ = 5 mV. Standard deviation of the stoichiometric composition of $Hg_{1-x}Cd_xTe$ substrate $\sigma(x)$ = 0.1%. V_G = 1.26 V. Average stoichiometric composition x=0.2105, T=60 K.

5. Conclusion

A mathematical model was developed to analyze the performance characteristics of IR FPAs based on the system 'IR photodiode – direct injection readout circuit'. The proposed mathematical model is based on the solution of the self-consistent problem for the current through photodiode and for the current integrated in the readout circuit, and also on the calculation of the noise charge Q(t) in terms of noise-current spectral density $S_i(\omega)$. Such an approach allows one to determine the main performance characteristics of thermography systems based on multi-element IR FPAs versus the gate voltage of photodetector channels, to calculate histograms $D^*(V_G)$, $I_{in}(V_G)$, and NETD as functions of non-uniformity of photoelectric parameters of photodiodes and silicon readout circuits, and to compare predicted performance characteristics of IR FPAs with experimental results.

The analysis of performance characteristic of multi-element FPAs can be performed with setting photodiode current-voltage characteristics either in analytical form ("classical"

photodiode model, analytical model of $Hg_{1-x}Cd_xTe$ photodiodes) or as an approximation of experimental current-voltage characteristics of photodiodes. The proposed approach will be helpful in identifying the main factors that limit the performance characteristics of multi-element IR FPAs, and in formulating requirements to photoelectric characteristics of IR photodiodes, design and electrophysical parameters of readout circuits, and requirements to silicon technology used to fabricate direct injection readout circuits enabling the achievement of required performance characteristics of multi-element IR FPAs and thermography system based on such FPAs.

6. References

Anderson W. (1981). Tunnel contribution to $Hg_{1-x}Cd_xTe$ and $Pb_{1-x}Sn_xTe$ p-n junction diode characteristics. *Infrared Physics*, Vol. 20, (1981), pp. 353-361

Anderson W. & Hoffman H. (1982). Field ionization of deep levels in semiconductors with applications to $Hg_{1-x}Cd_xTe$ p-n junctions. *J. Appl. Physics*, Vol. 53, N.12, (1982), pp.9130-9145

Bisotto S. et al. (2010). A 25μm pitch LWIR staring focal plane array with pixel-level 15-bit ADC ROIC achieving 2mK NETD. *Proc. of SPIE*, (2010) vol.7884, 7884oJ-1

Bluzer N. & Stehlik R. (1978). Buffered direct injection of photocurrents into charge-coupled devices. *IEEE Transaction on Electron Devices*, Vol.ED-25, No.2, (1978), pp.160-167

Buckingham M. (1983). Noise in Electronic Devices and Systems. *Ellis Horwood Ltd*, (1983)

D'Souza F. et al. (2002). 1/f noise in HgCdTe detectors. *Proc. SPIE "Infrared detectors and Focal plane arrays VII"*, No.4721, (2002), pp. 227-233

Felix P., et al. (1980). CCD readout of infrared hybrid focal plane arrays. *IEEE Transaction on Electron Devices*, Vol. ED-27, No.1, (1980), pp.175-188

Fowler B.l, Gamal A. & Yang D. (2000). Technical for pixel level analog to digital conversion. *Proc. SPIE*, Vol.3360, (2000), pp.124-138

Gopal V. (1996). Spatial noise limited NETD performance of a HgCdTe hybrid focal plane array. *Infrared physics and technology*, Vol.37, (1996), pp.313-320

Gumenjuk-Sichevska J. & Sizov F. (1999). Currents in narrow-gap photodiodes. *Semicond. Sci. Techn*. Vol. 14, (1999), pp.1124-1133

Gumenjuk-Sichevska J.; Karnaushenko D.; Lee I. & Polovinkin V. (2011). Infrared photodetectors based on the system $Hg_{1-X}Cd_XTe$ photodiode – direct-injection readout circuit. *Opto-electronics review* Vol.19, No.2, (2011), pp.63-70

Iwasa S. (1977). Direct coupling of five-micrometer (HgCd)Te photovoltaic detector and CCD multiplexer. *Optical engineering*. Vol. 16, N.3, (1977), pp. 233-236

Karnaushenko D.; Lee I. et al. (2010). Infrared focal plane arrays based on systems photodiode-direct injection readout circuits. *Opticheskii Zhurnal*, Vol. 77, No.9, (2010), pp.30-36

Krishnamurthy S. et al. (2006). Tunneling in long-wavelength infrared HgCdTe phodiodes. *Journal of Electronic Materials*, Vol. 35, No. 6, (2006), pp.1399-1402

Kunakbaeva G. & Lee I. (1996). Selection of the spectral range for infrared vision systems based on $Cd_xHg_{1-x}Te$ multielement photodiodes. *Optoelectronics, Instrumentation and Date Processing*, Vol.5, (1996), pp.19-26

Kunakbaeva G., Lee I. & Cherepov E. (1993). The system photodiode – direct-injection input CCD for multi-element FPAs. *Radiotekhnika i Electronika*, Vol.5, (1993), pp.922-930

Lee I. (2010). A new readout integrated circuit for long-wavelength IR FPA. *Infrared Physics and Technology*, Vol. 53, Issue 2, (2010), pp. 140-145

Longo J.T., et al.. (1978). Infrared focal plane in intrinsic semiconductors. *IEEE J. Solid State Circuits*, Vol. SC-13, N.1, (1978), pp.139-157

Martijn H.& Andersson J. (2000). On-chip analog to digital conversion for cooled infrared detector arrays. *Proc. SPIE "Infrared detectors and Focal plane arrays VI"*, Vol.4028, (2000), pp. 183-191

Mikoshima H. (1982). 1/f noise in n-channel silicon –gate MOS transistors. *IEEE Transaction on Electron Devices*, ED-29 – (1982), pp. 965-970

Overstraeten R., Declerck G. & Muls P. (1975). Theory of the MOS transistor in weak inversion – new method to determine the number of surface states. *IEEE Transaction on Electron Devices*, ED-22, (1975), pp. 282-288

Phillips J., Edwall D. & Lee D. (2002). Control of Very-Long-Wavelength Infrared HgCdTe Detector-Cutoff Wavelength. *Journal of Electronic Materials*, Vol. 31, No. 7, (2002), pp.664-668

Reimbold G. (1984). Modified 1/f trapping noise theory and experiments in MOS transistors biased from weak to strong inversion – influence of interface states. *IEEE Transaction on Electron Devices*, ED-31, (1984), pp. 1190-1198

Reimbold G. (1985). Noise associated with charge injection into a CCD by current integration through a MOS transistor. *IEEE Transaction on Electron Devices*, ED-32, (1985), pp. 871-873

Rogalski A. (2000). Infrared detectors. *Gordon and breach science publishers*, Canada, 2000

Sizov F. et al. (2006). Gamma radiation exposure of MCT diode arrays. *Semicond. Sci. Technol*., Vol. 21, (2006), pp. 356-363

Steckl A.& Koehler T. (1973). Theoretical analysis of directly coupled 8-12 μm hybrid IR CCD serial scanning. *Proc. Int. Conf. Application of CCD's*, (1973), pp.247-258

Steckl A. (1976). Infrared charge coupled devices. *Infrared Physics.* Vol. 16, (1976), pp. 65.

Takigawa H., Dohi M. & Ueda R. (1980). Hybrid IR CCD Imaging Arrays. *IEEE Transaction on Electron Devices*, Vol. ED-27, No.1, (1980), pp.146-150

Taubkin I. & Trishenkov M. (1993). Minimum temperature difference resolvable with the IR imaging method. *Opticheskii Zhurnal*, Vol. 5, (1993), pp. 20-23

Tobin S., Iwasa S. & Tredwell T. (1980). 1/f noise in (Hg, Cd)Te photodiodes. *IEEE Transaction on Electron Devices*. ED-27 (1980), pp. 43-48

Vasilyev V. et al. (2010). 320.256 HgCdTe IR FPA with a built-in shortwave cut-off filter. *Opto−Electron. Rev*., Vol.18, No. 3, (2010), pp.236-240

Yoshino J. et al. (1999). Studies of relationship between deep levels and RA product in mesa type HgCdTe devices. *Opto-Electronics Review*, Vol. 7, (1999), pp.361-367

Zhou Z., Pain B., et al. (1996). On-focal-plane ADC: Recent progress at JPL. *Proc. SPIE,* "*Infrared readout electronics III*", Vol. 2745, (1996), pp.111-122

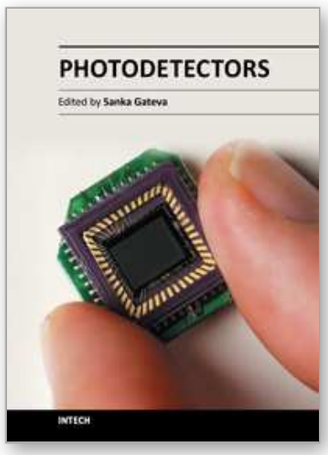

Photodetectors

Edited by Dr. Sanka Gateva

ISBN 978-953-51-0358-5
Hard cover, 460 pages
Publisher InTech
Published online 23, March, 2012
Published in print edition March, 2012

In this book some recent advances in development of photodetectors and photodetection systems for specific applications are included. In the first section of the book nine different types of photodetectors and their characteristics are presented. Next, some theoretical aspects and simulations are discussed. The last eight chapters are devoted to the development of photodetection systems for imaging, particle size analysis, transfers of time, measurement of vibrations, magnetic field, polarization of light, and particle energy. The book is addressed to students, engineers, and researchers working in the field of photonics and advanced technologies.

How to reference

In order to correctly reference this scholarly work, feel free to copy and paste the following:

I.I. Lee and V.G. Polovinkin (2012). Mathematical Modeling of Multi-Element Infrared Focal Plane Arrays Based on the System ‘Photodiode – Direct-Injection Readout Circuit’, Photodetectors, Dr. Sanka Gateva (Ed.), ISBN: 978-953-51-0358-5, InTech, Available from: http://www.intechopen.com/books/photodetectors/mathematical-modeling-of-multi-element-infrared-focal-plane-arrays-based-on-the-system-photodiode-di

INTECH
open science | open minds

InTech Europe
University Campus STeP Ri
Slavka Krautzeka 83/A
51000 Rijeka, Croatia
Phone: +385 (51) 770 447
Fax: +385 (51) 686 166
www.intechopen.com

InTech China
Unit 405, Office Block, Hotel Equatorial Shanghai
No.65, Yan An Road (West), Shanghai, 200040, China
中国上海市延安西路65号上海国际贵都大饭店办公楼405单元
Phone: +86-21-62489820
Fax: +86-21-62489821

IntechOpen